Mineralium Deposita (2023) 58:337–358
https://doi.org/10.1007/s00126-022-01128-w

ARTICLE

Pyrite trace element and S-Pb isotopic evidence for contrasting sources of metals and ligands during superimposed hydrothermal events in the Dongping gold deposit, North China

Huan Li[1] · Da-Peng Zhu[1] · Thomas J. Algeo[2,3,4] · Ming Li[2] · Wei-Cheng Jiang[5] · She-Fa Chen[1] · Safiyanu Muhammad Elatikpo[1]

Received: 16 December 2020 / Accepted: 15 June 2022 / Published online: 27 June 2022

Abstract

The Dongping gold deposit, located near the northern margin of the North China Craton, contains ore bodies spatially associated with the Devonian Shuiquangou syenite, Cretaceous Shangshuiquan granite, and Archean metamorphic rocks. Major and trace elements and S–Pb isotopes of pyrite from two stages of gold-quartz veins and wall rocks were used to constrain the composition of hydrothermal fluids and metal sources. Stage-1 (early) pyrites are euhedral to subhedral, medium- to coarse-grained, and have low gold contents. Py1a is homogeneous with few fractures, whereas Py1b, which occurs on the edges of Py1a, is porous and has higher metal contents. Stage-2 (late) pyrites are mostly anhedral to subhedral and have smaller grain sizes and higher gold contents than Stage 1. Py2a occurs with sulfide minerals such as galena and chalcopyrite, and Py2b is porous and has the highest gold content (up to 1839 ppm) and smallest grain size. All pyrite samples yield negative $\delta^{34}S$ values (−7.5 to −3.5‰), reflecting oxidized conditions during mineralization. The ~ 2‰ decrease in $\delta^{34}S$ values from Stage 1 (−4.3‰, −4.9‰) to Stage 2 (−7.0‰, −6.4‰) may reflect a change in the fluid source and/or an increase in fO_2. The Pb isotope composition of Stage-1 pyrite is suggestive of a mantle source similar to that of the Shuiquangou syenite, whereas Stage-2 pyrite has more radiogenic Pb isotopic compositions suggestive of an Archean metamorphic source. Combined with previous studies, our trace element and isotopic results indicate that the two stages of pyrite had different sources, with Stage-2 pyrite being more strongly influenced by metasedimentary rocks. We propose that the early stage of low-grade gold mineralization was related to emplacement of the Devonian Shuiquangou syenite, whereas the late stage of high-grade gold mineralization was related to emplacement of the Cretaceous Shangshuiquan granite and leaching of gold from Archean metamorphic rocks.

Keywords Fluid evolution · Ore mineralization · Shuiquangou · Shangshuiquan · LA-ICP-MS · Gold ore

Introduction

The well-known Dongping gold deposit, with a gold reserve of about 100 tons, is located on the northern margin of the North China Craton (NCC) (Fig. 1a, b). It is thought to be genetically related to alkaline magmatism (Mao et al. 2003)

Editorial handling: D. Dolejs

✉ Huan Li
lihuan@csu.edu.cn

[1] Key Laboratory of Metallogenic Prediction of Nonferrous Metals and Geological Environment Monitoring, Ministry of Education, School of Geosciences and Info-Physics, Central South University, Changsha 410083, China

[2] School of Earth Resources, State Key Laboratory of Geological Processes and Mineral Resources, China University of Geosciences, Wuhan 430074, China

[3] State Key Laboratory of Biogeology and Environmental Geology, China University of Geosciences, Wuhan 430074, China

[4] Department of Geology, University of Cincinnati, Cincinnati 45221-0013, USA

[5] Department of Earth and Environmental Sciences, Macquarie University, Sydney, NSW 2109, Australia

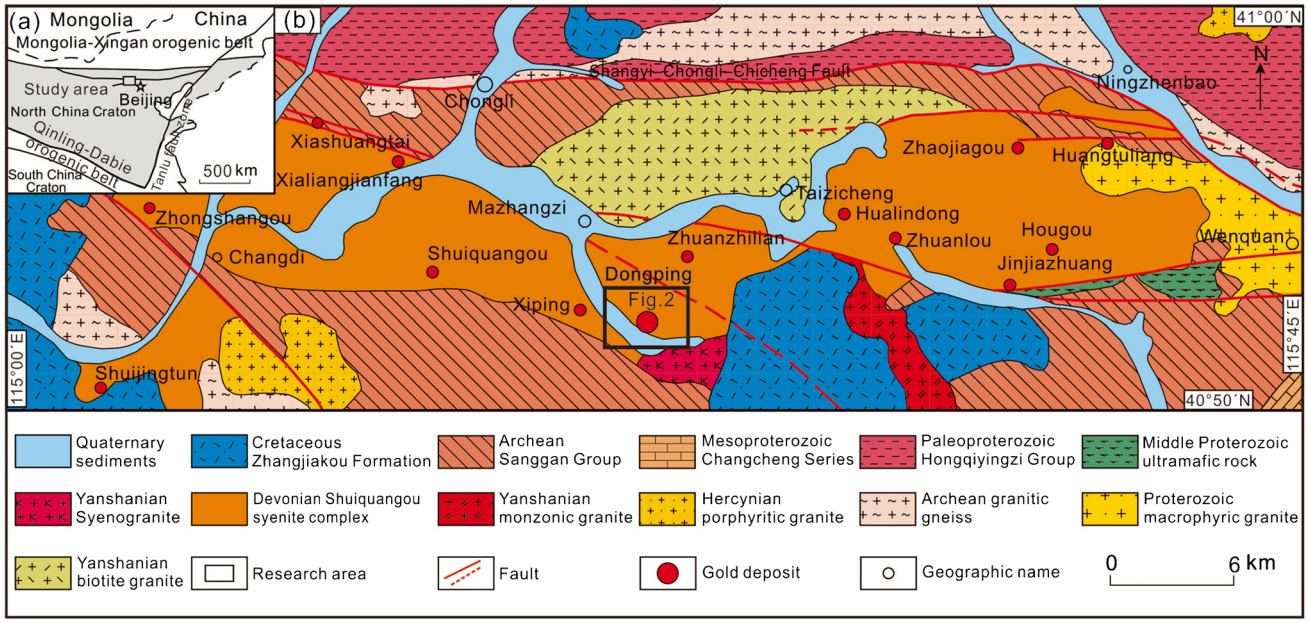

Fig. 1 **a** Location of the study area (after Zhou and Wang 2012); **b** simplified geological map of the Dongping region in Chongli County, Hebei Province (after Song and Zhao 1996; Li et al. 2012a, b, c; Gao et al. 2015)

as auriferous quartz veins containing disseminated sulfides are hosted mainly by the Late Paleozoic Shuiquangou syenite complex and surrounding Archean metamorphic rocks (Fig. 2; Cook et al. 2009; Cisse et al. 2017; Li et al. 2018a). Dongping has been referred to as an "oxidized intrusion-related gold deposit" that is rich in Te, poor in Cu and Zn, and associated with oxidized minerals and potassic alteration (Helt et al. 2014). Several similar gold deposits have been found in this region (e.g., Hougou and Huangtuliang) and are referred to as "Dongping-type" gold deposits (Bao et al. 2016). Previous researchers have identified two stages of mineralization (~ 380 Ma and ~ 140 Ma; Miao et al. 2002; Bao et al. 2014; Cisse et al. 2017; Li et al. 2018a; Wang et al. 2019b), but the sources of ore-forming metals and the history of fluid evolution of this deposit are still controversial (Nie 1998; Fan et al. 2001; Mao et al. 2003; Bao et al. 2016; Wang et al. 2019a). Furthermore, the relationship of gold mineralization to the host rock is also unclear (Nie et al. 2004; Bao et al. 2014). Previous studies claimed that the Dongping gold deposit has a close relationship with the Shuiquangou syenite (Bao et al. 2014; Jiang and Nie 2000; Li et al. 2000; Luo et al. 2001; Miao et al. 2002), and trace element data in pyrite have been studied in this context (Cook et al. 2009). However, more recent studies speculated that other granitic rocks, such as the Shangshuiquan granite and Archean metamorphic rocks, also provided ore-forming materials at different stages of ore deposit evolution (Li et al. 2018a). Previous work mainly used bulk-rock analysis for sulfur and lead isotopic studies in sulfides (Nie 1998; Bao et al. 2016), which cannot clearly distinguish different pyrite generations and thus is difficult to compare the fluid features of the two mineralization stages.

Pyrite is one of the most ubiquitous and useful of auriferous minerals in gold deposits. It can provide information on ore-forming processes and ligand and metal sources, and its association with galena, sphalerite, and other sulfides can be used to assess the geochemistry of coeval hydrothermal fluids (Barker et al. 2009; Koglin et al. 2010; Deditius et al. 2014; Tanner et al. 2016). Laser ablation inductively coupled plasma mass spectrometry (LA–ICP–MS) is widely used for in situ analysis to accurately measure the trace element contents in pyrite (Cook et al. 2009; Large et al. 2009; Sung et al. 2009; Bi et al. 2011;Zhang et al. 2014; Yang et al. 2016). Pyrite usually contains a diverse assemblage of trace elements (Co, Ni, Se, Te, Hg, Tl, Au, Ag, Cu, Pb, Zn, and Bi) and isotopes (Pb and S) at concentrations that are within the detection limits of LA–ICP–MS (Reich et al. 2005, 2013; Large et al. 2007; Deditius et al. 2009, 2014; Cook et al. 2013). Gold in pyrite usually occurs in the form of submicroscopic ("invisible") gold (< 100 nm; nanoparticle or lattice-bound gold), as micron-scale mineral inclusions, distributed within pyrite fractures, or between grains in the form of native gold (Morey et al. 2008; Large et al. 2009; Pokrovski et al. 2009; Deditius et al. 2011). Native gold may precipitate directly from hydrothermal fluids, or it may form by re-mobilization of earlier-formed pyrite within hydrothermal veins during later mineralization stages (Cook et al. 2009; Sung et al. 2009; Morishita et al. 2018). Pyrite appears to be the dominant gold carrier in

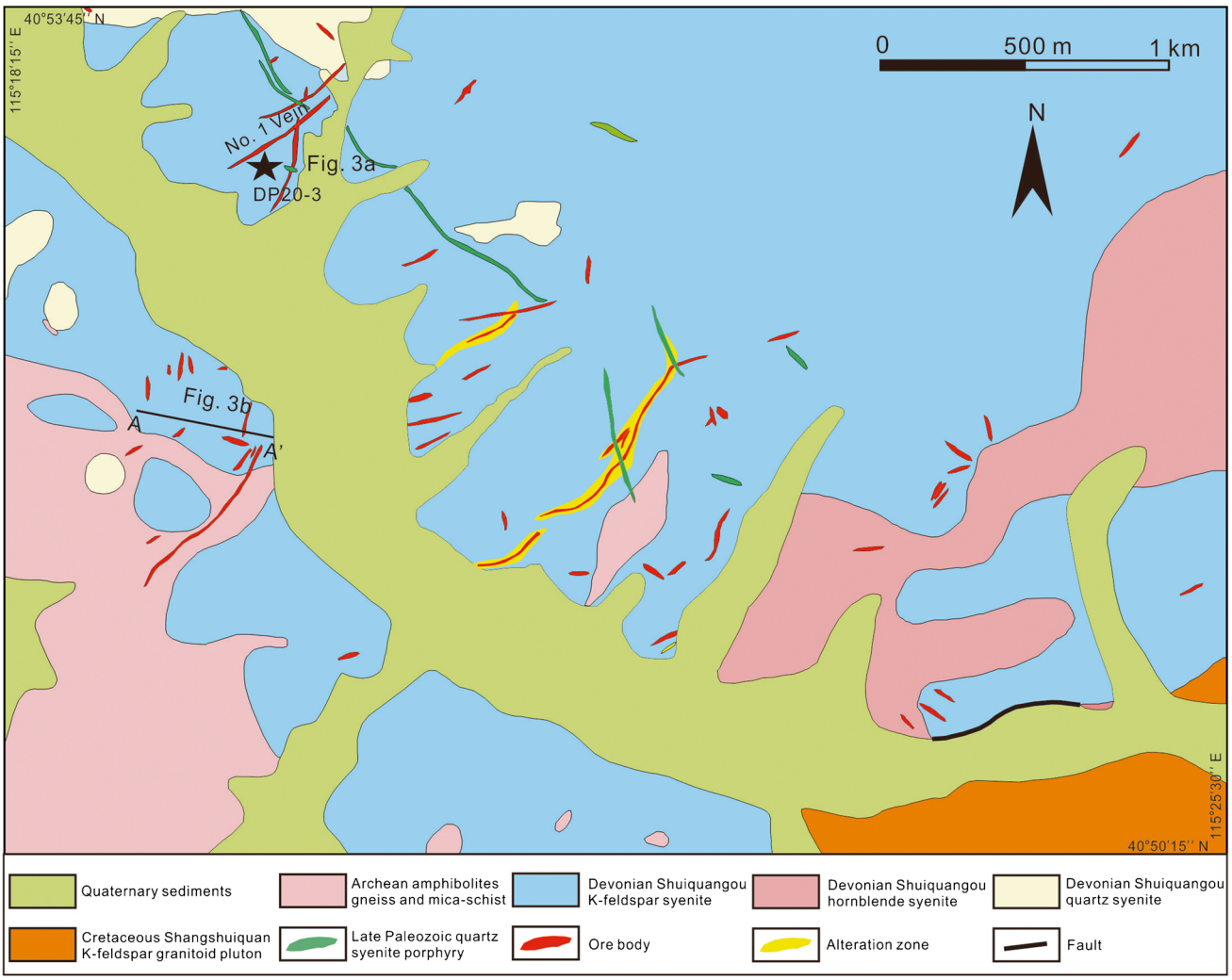

Fig. 2 Simplified geological map of the Dongping gold deposit (modified after Li et al. 2010)

the Dongping gold deposit in both mineralization stages, suggesting that pyrite geochemistry can provide useful information about the genesis of this deposit.

In this study, the textural and geochemical characteristics of pyrite that formed during the two main mineralization stages were documented using optical petrography, electron probe micro analysis (EPMA), LA–(MC)–ICP–MS trace element, and in situ S and Pb isotopic analyses. The results show that systematic differences in texture and geochemistry exist among the four different types of pyrite at Dongping, which implies variable sources of ore-forming materials and a complicated fluid evolution history. We aim to use pyrite compositions to infer gold mineralization sources/types, identify gold occurrence and precipitation mechanisms, and gain insights into the genesis of the Dongping gold deposit.

Regional geology

The Dongping gold deposit is situated near the northern margin of the North China Craton (NCC; Fig. 1a), about 10 km to the south of the Shangyi–Chongli–Chicheng fault (Fig. 1b). The exposed stratigraphic units in the Dongping region include the Archean Sanggan Group, Paleoproterozoic Hongqiyingzi Group, Mesoproterozoic Changcheng Series, Cretaceous Zhangjiakou Formation, and Quaternary sediments (Fig. 1b). The Archean Sanggan Group consists mainly of amphibolite, granulite, and gneiss derived from metamorphism of mafic to felsic volcaniclastic rocks and clastic rocks. The Paleoproterozoic Hongqiyingzi Group is composed of marble, quartzite, amphibolite, and gneiss. The Mesoproterozoic Changcheng Series consists of shallow-marine siliciclastic

and carbonate rocks and terrestrial siliciclastics that are overlain by minor basalt and felsic volcanic rocks that contain stromatolite and microplant fossils. The Cretaceous Zhangjiakou Formation is composed of rhyolite, sandstone, conglomerate, and pyroclastic rocks.

Igneous rocks ranging from Archean to Cretaceous in age are widely distributed in the Dongping region (Figs. 1b and 2). They include Neoarchean to Paleoproterozoic granodiorite and monzonite (Liu et al. 2006; Li et al. 2012a, b, c), the 380-Ma Devonian Shuiquangou syenite (Luo et al. 2001; Bao et al. 2014), the Cretaceous 140-Ma Shangshuiquan granite, and the Zhangjiakou Formation volcanic rocks (Jiang et al. 2007; Li et al. 2012a, b, c).

The study region was affected by Late Jurassic–Early Cretaceous contraction related to the collision and amalgamation of the Siberia Block and Mongolia-North China Block and subsequent extension caused by rollback of the northwest-dipping Pacific slab beneath North China (Zhang et al. 2010, 2011). Structures in the Dongping region include E–W-, NW-, WNW-, NE-, and N-S-trending faults and parallel folds (Figs. 1b and 2). One of the most significant tectonic discontinuities is the E–W-trending Shangyi-Chongli-Chicheng fault zone, a mantle-penetrating fault (Zhang et al. 2007) that controlled emplacement of the Shuiquangou syenite complex and the distribution of gold mineralization (Jiang and Nie 2000; Li et al. 2000). It is dominated by multistage, ductile to brittle thrusting and is seismically active (Ma and Zhao 1999).

Deposit geology

The Dongping gold deposit is located at 40°50′15″–40°53′45″N latitude and 115°18′15″–115°25′30″W longitude, in the southeastern part of Chongli County, Hebei Province. It consists of ore bodies distributed over an area of about 40 km^2 (Fig. 2). The Jianhegou Formation of the Archean Sanggan Group is exposed in the southwestern corner of the mining district (Fig. 2) and is composed mainly of hornblende-bearing gneiss and amphibolite with minor biotite schist and metamorphosed granitoids. The Devonian Shuiquangou syenite complex occupies an area of about 400 km^2 and is distributed along an E-W axis with a length of ~ 56 km and a width of 6–8 km (Fig. 1b; Song 1991). It was emplaced into Jiangouhe Formation metamorphic rocks of the Archaean Sanggan Group and is unconformably overlain by Lower Cretaceous Zhangjiakou Group volcanic tuffs in the southeastern corner of the mining district (Fig. 2). The syenite complex is dominated by K-feldspar syenite, hornblende syenite, and quartz syenite (Fig. 2). Magmatic zircons from the syenite complex yielded a concordant age of 382.8 ± 3.3 Ma by LA–ICP–MS U–Pb dating (Li et al. 2010). The Cretaceous Shangshuiquan granite, which has been classified as an alkali granite (Jiang et al. 2009; Cisse et al. 2017), crops out in the southeastern part of the mining district (Fig. 2). It was emplaced into the Devonian Shuiquangou syenite in the north and west, Archean Sanggan Group metamorphic rocks in the south, and Cretaceous Zhangjiakou Formation volcanic rocks in the east. At depth, the Shangshuiquan pluton extends towards the northwest beneath the Dongping ore bodies, as revealed by drilling (Cisse et al. 2017). LA–ICP–MS and SHRIMP zircon U–Pb dating yielded ages of 136–142 Ma for the Shangshuiquan granitic pluton (Miao et al. 2002; Cisse et al. 2017; Li et al. 2018a).

Gold mineralization was mainly controlled by several generations of faults and fractures (Song et al. 1996; Jiang and Nie 2000), particularly NW-striking dextral conjugate faults and NE- to NNE-trending sinistral faults (Fig. 2). It is commonly believed that dilatant faults provided channels for the migration of hydrothermal fluids in the Dongping deposit (Li 1999; Bao et al. 2016).

There are more than 70 gold veins (ore bodies) in the district that vary in size and geometry. The dominant NE- and NNE-trending veins can be subdivided into nine vein systems (mineralization zones), with gaps between them ranging from 400 to 800 m (Fig. 2). Among them, the No. 1 and No. 70 vein systems host > 60 ore bodies and ~ 80% of the total gold reserves of the Dongping deposit (Bao et al. 2014). The gold ores in the entire deposit have an average grade of 6 g/t Au. The No. 1 and No. 70 vein systems partially overlap and are more than 750 m long and 130–300 m wide and extend about 800 m downward. Individual ore bodies (veins) are 200–400 m long and 0.5–40 m wide and extend 100–600 m downward (Fig. 3a, b). They strike 10–40° and dip 20–55° to the NW.

Two gold mineralization events

There are various ore types in the Dongping gold deposit as well as quartz veins and silicified and calcitized rocks (Figs. 4a–i). Quartz veins occur mainly in the upper part of the ore bodies and consist of quartz, pyrite, and native gold with minor galena and sphalerite. Silicified and calcitized rocks occur mainly in the lower part of the ore bodies and contain quartz, chalcopyrite, and pyrite veins, in which galena and sphalerite can also be observed. In places, silicified and potassically altered rocks occur in contact with quartz veins. The ores are composed mainly of quartz and feldspar (68.6–98.7%), with only subordinate metallic minerals. Sphalerite and chalcopyrite account only for 1.3–1.4% of the ore, and the total content of sulfur is less than 5%, making the quartz veins sulfur-poor. Minor sericite, calcite, barite, epidote, and clay minerals are present locally (Gao et al. 2017).

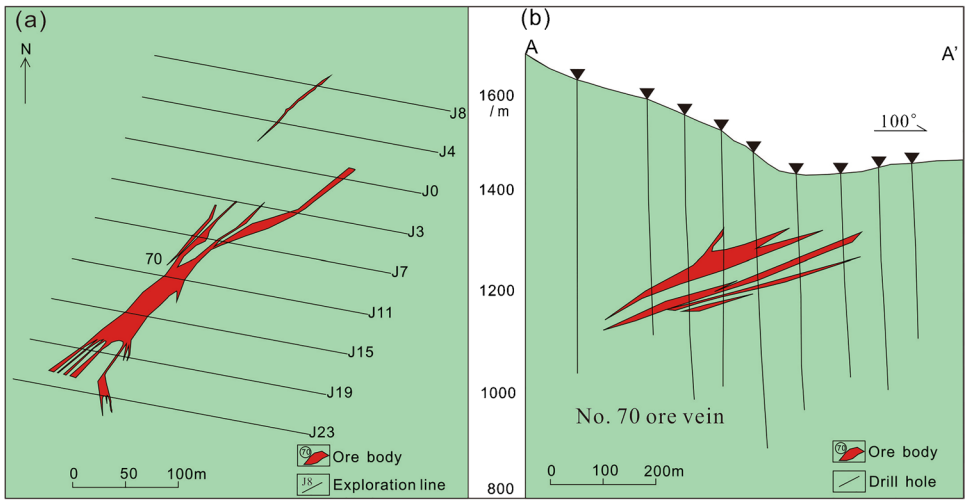

Fig. 3 (**a**) Plan view of the No. 70 ore body; **b** cross-section of the No. 70 ore body (after Zijin Mining in Chongli, 2011)

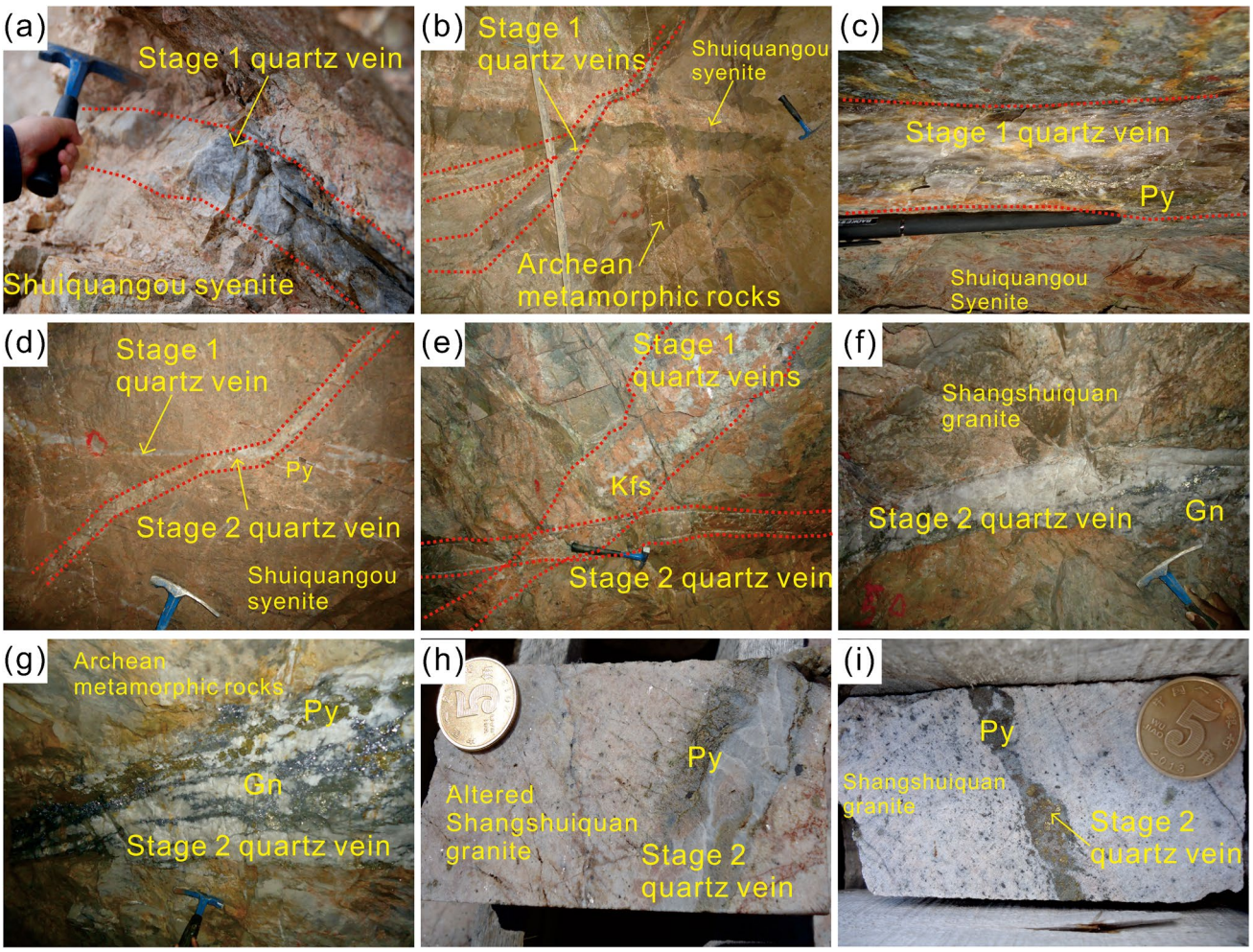

Fig. 4 Field and underground photographs of two stages of auriferous quartz veins–associated wall rocks in the Dongping gold deposit. **a** Stage-1 Gy quartz veins in syenite; **b** Stage-2 Gy quartz veins in syenite and Archean metamorphic rocks; **c** disseminated pyrite in Stage-1 quartz veins; **d–e** two stages of cross-cutting quartz veins in syenite; **f** Stage-2 quartz veins in Shangshuiquan granite; **g** Stage-2 milky gold-rich quartz-polymetallic sulfide veins in Archean metamorphic rocks; **h–i** Stage-2 gold-bearing quartz-polymetallic sulfide veins in Shangshuiquan granite. Qtz: quartz; Kfs: K-feldspar; Py: pyrite; Gn: galena; Au: gold

Two mineralization stages can be identified from field observations. Stage 1 produced gray quartz veins in potassically altered wall rocks associated with emplacement of the Shuiquangou syenite at ca. 380 Ma, as dated by hydrothermal zircon U–Pb geochronology (Miao et al. 2002; Cisse et al. 2017; Li et al. 2018a). These gray, narrow (mostly from 5 to 50 cm in width) auriferous quartz veins (Fig. 4a–e) contain coarse-grained cubic pyrite (Fig. 5a–d). These veins show characteristics of pervasive K-feldspathization and silicification. The gold is generally fine-grained and rarely visible in hand specimens.

Stage 2 polymetallic sulfide–quartz precipitation formed milky quartz veins (Fig. 4f–i) related to intrusion of the Shangshuiquan granite dated at 140 Ma, as dated by hydrothermal zircon and garnet U–Pb geochronology (Miao et al. 2002; Cisse et al. 2017; Li et al. 2018a; Fan et al. 2021). These veins cut through (Fig. 4d, e) or parallel to the first-stage quartz veins, containing pyrite, galena, chalcopyrite, and high-grade gold (Fig. 5e–i). These veins generally have higher gold contents with visible gold grains (Fig. 5g, h). Close to these veins, abundant sulfides are found in the Shangshuiquan granite and Archean metamorphic rocks (Li et al. 2018a). This stage hosts the vast majority of gold in the mining district (Miao et al. 2002; Cook et al. 2009; Bao et al. 2016; Fan et al. 2021).

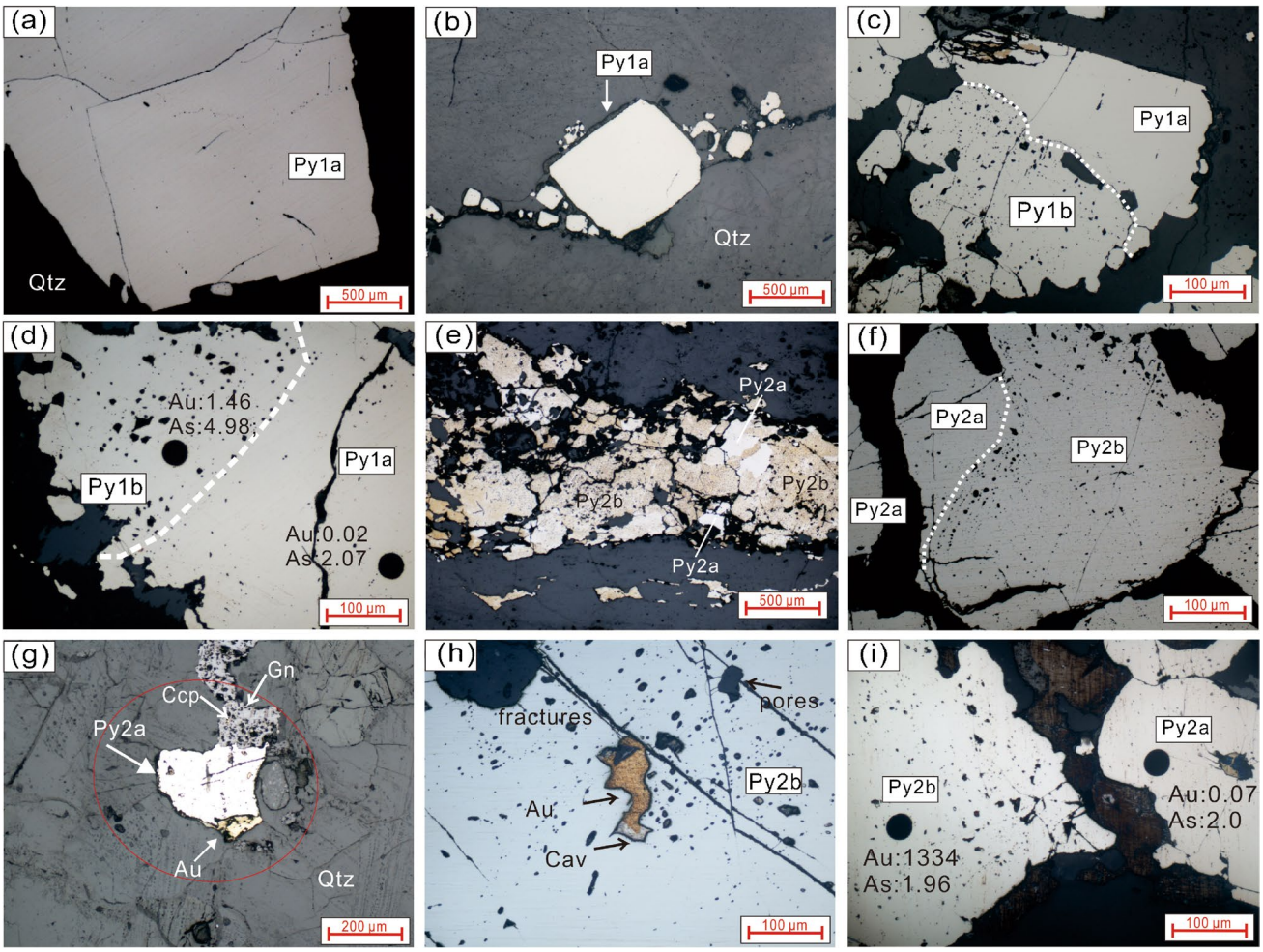

Fig. 5 Microphotographs showing textures and features of Stage-1 and Stage-2 pyrite. **a**, **b** Coarse-grained, euhedral to subhedral Py1a that is homogeneous and lacking pores; **c**, **d** porous Py1b develops on the edge of Py1a, suggesting replacement of massive pyrite (Py1a) by porous pyrite (Py1b); **e**, **f** Py2 shows similar textural relation between Py2a (massive and homogeneous) and Py2b (porous); **g** Py2a contains native gold and is contemporaneous with galena, chalcopyrite, and other sulfide minerals; **h** native gold in fractures and pores of Py2b, which is often associated with telluride (e.g., calaverite); **i** porous Py2b contains more gold than homogeneous Py2a. Qtz: quartz; Kfs: K-feldspar; Py: pyrite; Gn: galena; Ccp: chalcopyrite; Cav: calaverite; Au: gold. Au and As contents shown in **d** and **i** are in ppm

Sampling and analytical methods

Sample preparation

Ten representative samples were collected from the Stage-1 quartz-pyrite veins (dated at ~ 380 Ma; Li et al. 2018a), Stage-2 quartz-polymetallic sulfide veins (dated at ~ 140 Ma; Fan et al. 2021), and wall rocks in four mine levels (at depths of − 1144 m, − 1184 m, − 1344 m, and − 1390 m; Fig. 3). Thin sections were made from these samples for petrographic, textural, and in situ geochemical, isotopic, and geochronological analyses.

EPMA analysis

Electron microprobe analysis of pyrite was carried out using a Shimadzu EPMA-1720H equipped with an energy dispersive spectroscopy (EDS) system at the Key Laboratory of Metallogenic Prediction of Nonferrous Metals and Geological Environment Monitoring, Ministry of Education based at School of Geosciences and Info-Physics, Central South University (China). The operating conditions of the electron microprobe were an accelerating voltage of 15 kV, a beam current of 20 nA, and an electron beam diameter of ~ 5 μm that was adjusted based on the size of pyrite grains. The following eight elements were analyzed: Fe (Kα), S (Kα), As (Lα), Co (Kα), Ni (Kα), Pb (Mα), Zn (Kα), and Ag (Lα). Mineral and metal standards used for elemental calibrations included chalcopyrite (Fe, S), arsenopyrite (As), metallic cobalt (Co), pentlandite (Ni), galena (Pb), sphalerite (Zn), and metallic silver (Ag) (Liu et al. 2017). All data were corrected using a standard ZAF routine, and the minimum detection limits of the elements are ≤ 0.01 wt.%.

LA–ICP–MS trace element analysis

Trace element analysis of pyrite was conducted by laser ablation inductively coupled plasma mass spectrometry (LA–ICP–MS) at the State Key Laboratory of Geological Processes and Mineral Resources, China University of Geosciences (Wuhan). Detailed operating conditions of the laser ablation system, the ICP–MS instrument, and data reduction are given in Zong et al. (2017). Laser sampling was performed using a GeolasPro laser ablation system that consists of a COMPexPro 102 ArF excimer laser, with a wavelength of 193 nm and a maximum energy of 200 mJ, and a MicroLas optical system. An Agilent 7700e ICP–MS instrument was used to acquire ion-signal intensities. Helium was used as the carrier gas and argon as the make-up gas, with mixing via a T-connector before entering the ICP-MS. A "wire" signal smoothing device was present in this laser ablation system (Hu et al. 2015). The spot size and frequency of the laser were set at 40 μm and 10 Hz, respectively. Trace element composition of sulfides was calibrated against various reference materials (NIST 610 and NIST 612), and no internal standard was used (Liu et al. 2008). The sulfide reference material of MASS-1 (USGS) was used as the unknown sample to verify the accuracy of the calibration method. Each analysis incorporated a background acquisition of approximately 20–30 s followed by 50 s of data acquisition for the sample. An Excel-based software ICP–MS DataCal was used to perform off-line selection and integration of background and analyzed signals, as well as time-drift corrections and quantitative calibrations of trace element data (Liu et al. 2008). Details of LA-ICP-MS data quality control and related matters are presented in Electronic Supplementary Material (ESM 1).

In situ S isotope analysis

In situ sulfur isotope analysis of pyrite was performed on a Neptune Plus MC–ICP–MS (Thermo Fisher Scientific, Germany) equipped with a Geolas HD excimer ArF laser ablation system (Coherent, Germany) at the Sample Solution Analytical Technology Co., Ltd. (Wuhan, China). In the laser ablation system, helium was used as the carrier gas in the ablation cell and subsequently mixed with argon (the makeup gas). The single-spot ablation mode was used. A large spot size (44 μm) and slow pulse frequency (2 Hz) were used to avoid down-hole fractionation effects (Fu et al. 2016). During each analysis, 100 laser pulses were completed. A new signal-smoothing device was used downstream from the sample cell to efficiently eliminate short-term variation of the signal, especially for the slow-pulse frequency condition (Hu et al. 2015). The laser fluence was kept constant at ~ 5 J/cm^2. The Neptune Plus was equipped with nine Faraday cups fitted with $10^{11}\Omega$ resistors. Isotopes ^{32}S, ^{33}S, and ^{34}S were collected in Faraday cups in static mode. The newly designed X skimmer cone and Jet sample cone in the Neptune Plus were used to improve signal intensity. Nitrogen (4 ml/min) was added to the central gas flow to reduce polyatomic interferences. All measurements were performed using medium resolution with a revolving power (as defined by a peak edge width ranging from 5 to 95% of the full peak height) greater than 5000×. A standard-sample bracketing method (SSB) was employed to correct for instrumental mass fractionation. To avoid matrix effects, a pyrite standard PPP-1 was chosen as reference material for correcting the natural pyrite samples. The reference values for this standard relative to Vienna Canyon Diablo Troilite (VCDT) were reported by Fu et al. (2016). In addition, in-house standards, including a pyrrhotite SP-Po-01 ($\delta^{34}S_{VCDT} = +1.4 \pm 0.4‰$), a chalcopyrite SP-CP-01 ($\delta^{34}S_{VCDT} = +5.5 \pm 0.3‰$), and two synthetic Ag_2S standards IAEA-S-2 ($\delta^{34}S_{VCDT} = +22.6 \pm 0.39‰$) and IAEA-S-3 ($\delta^{34}S_{VCDT} = -32.2 \pm 0.45‰$), were analyzed repeatedly as

unknowns to verify the accuracy of the method. Details of the in situ S isotopic ratio analytical procedures were described by Fu et al. (2016).

In situ Pb isotope analysis

In situ lead (Pb) isotope analysis of pyrite was performed on the same MC-ICP-MS instrument at the State Key Laboratory of Geological Processes and Mineral Resources, China University of Geosciences (Wuhan). During laser ablation, helium carrier gas in the ablation cell was mixed with argon after the ablation cell. The spot diameter ranged from 44 to 90 μm dependent on Pb signal intensity. The pulse frequency was 4–10 Hz, but the laser fluence was kept constant at ~ 5 J/cm^2. A new signal-smoothing and mercury-removing device was used downstream from the sample cell to efficiently eliminate the short-term variation of the signal and to remove mercury from the background and sample aerosol particles (Hu et al. 2015). The Neptune Plus was equipped with nine Faraday cups fitted with 10^{11} Ω resistors. Isotopes ^{208}Pb, ^{207}Pb, ^{206}Pb, ^{204}Pb, ^{205}Tl, ^{203}Tl, and ^{202}Hg were collected in Faraday cups using static mode. The mass discrimination factor for Pb was determined using a Tl solution, nebulized at the same time as the sample, and an Aridus II desolvating nebulizer. The mass fractionation of Pb isotopes was exponentially corrected by ^{205}Tl/^{203}Tl. The optimized values of ^{205}Tl/^{203}Tl were calibrated from measuring two Pb isotope standards, MASS-1 (USGS) and Sph-HYLM (sphalerite, in-house), and were used to replace the natural Tl isotopic composition for the mass fractionation correction of Pb isotopes. The ^{202}Hg signal was used to correct the remaining ^{204}Hg interference on ^{204}Pb, using the natural ^{202}Hg/^{204}Hg ratio (0.230). In addition, the mass fractionation of ^{204}Hg/^{202}Hg was corrected by the ^{205}Tl/^{203}Tl normalization. In this case, we assumed identical mass fractionation factors for ^{204}Hg/^{202}Hg and ^{205}Tl/^{203}Tl. Standard Sph-HYLM was used to monitor the precision and accuracy of the measurements after ten sample analyses, over the entire period of analysis. The obtained accuracy is estimated to be equal to or better than ± 0.2‰ for ^{208}Pb/^{204}Pb, ^{207}Pb/^{204}Pb, and ^{206}Pb/^{204}Pb compared to the solution value determined by MC–ICP–MS, with a typical precision of 0.4‰ (2σ). More details of the in situ Pb isotopic ratio analysis are described in Zhang et al. (2016).

Analytical results

Texture and stages of pyrite

Based on field observations, petrographic, and mineralogical study, pyrite from mineralized quartz veins and adjacent rocks can be assigned to two stages (Py1 and Py2), and the pyrite of each stage can be further assigned to one of two substages (Py1a and Py1b; Py2a and Py2b).

The early-stage pyrite (Py1) is associated with gray-colored, gold-poor pyrite–quartz veins (Stage-1 quartz veins; Fig. 4a–d). It is medium- to coarse-grained and euhedral to subhedral, with cubic or pyritohedral shapes (Fig. 5a, b), and in some cases occurs as large individual crystal in the quartz veins. The Py1 crystals vary from < 10 to 800 μm in size, and some are larger than 2 mm (Fig. 5a). They commonly contain microfractures and holes on their surfaces, and some are homogeneous (Fig. 5a, b). Py1a and Py1b are distinguished based on textural relationships: Py1a is massive and euhedral and possesses a homogeneous characteristic (Fig. 5a, b), whereas Py1b is porous and developed on the edge of Py1a, showing a replacement texture (Fig. 5c, d).

Late-stage pyrite (Py2) occurs in milky, gold-rich, polymetallic sulfide–quartz veins and adjacent wall rocks (Fig. 4g, h, i). Py2 is anhedral to subhedral and exhibits grain sizes ranging mostly from 1 to 200 μm and occasionally up to 300 μm (Fig. 5e–i). The Py2 crystals have a close paragenetic relationship with galena, chalcopyrite, and other sulfide minerals (Fig. 5g). Free gold (Fig. 5g, h) occurs in some disseminated, porous, coarse-grained, and anhedral pyrite grains. Py2a and Py2b are also distinguished based on textural relationships: Py2a is relatively larger, homogeneous, and associated with sulfide minerals, whereas Py2b is porous and has a smaller grain size and higher gold content (Fig. 5e–i).

Major element composition of pyrite analyzed by EPMA

The major element composition of pyrites (Py1a, Py1b, Py2a, and Py2b) was analyzed in 10 representative samples by EPMA (ESM 2 Table 1). The abundance and correlations between these elements are shown in Fig. 6. Sulfur, Fe, Co, and As were uniformly above the detection limit (dl), whereas elements such as Ni, Ag, Cu, Zn, and Pb were sometimes below the dl (ESM 2 Table 1).

Although Stage-1 and Stage-2 pyrites have similar chemical compositions, there are some significant differences. The Fe content range of Py1 (44.7–46.9 wt%) is lower than that of Py2 (45.4–47.6 wt%). Average Fe contents generally increase through the sequence (Py1a 45.8 wt%, Py1b 46.1 wt%, Py2a 46.6 wt%, Py2b 46.4 wt%) (Fig. 6a). The average S contents of Py1 and Py2 are effectively identical (Py1a 53.4 wt%, Py1b 53.4 wt%, Py2a 53.3%, Py2b 53.3 wt%) (Fig. 6b). The average As contents of Py1 and Py2 are similar (Py1a 0.19 ± 0.02 wt%, Py1b 0.2 ± 0.03 wt%, Py2a 0.2 ± 0.02 wt%, Py2b 0.19 ± 0.02 wt%) (Fig. 6b). The average Cu contents of Py1 (Py1a 0.028 ± 0.020 wt%, Py1b 0.030 ± 0.030 wt%) are slightly lower than those of Py2 (Py2a 0.031 ± 0.020 wt%, Py2b 0.032 ± 0.020wt%) (Fig. 6c).

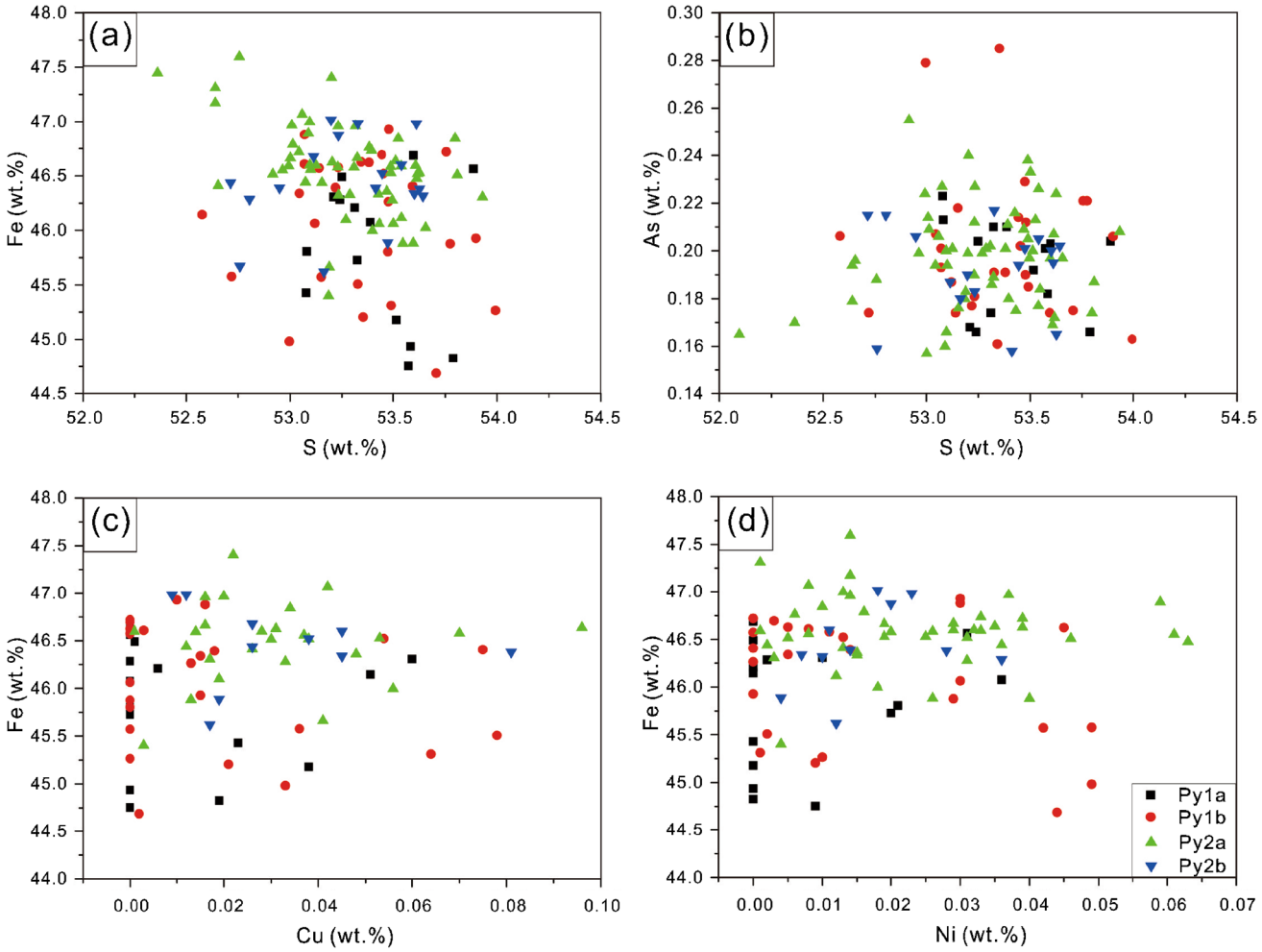

Fig. 6 Major element compositions analyzed by using EPMA. **a** Fe–S plot shows a negative correlation from Py1a to Py2b, and higher Fe contents for Py2a and Py2b relative to Py1a and Py1b; **b** As–S plot shows no distinction among the four types of pyrite; **c** the Fe–Cu and **d** the Fe–Ni plots do not show any correlations, and the distributions of the four types of pyrite are similar

The average contents of Ni in Py1 (range: dl–0.085 wt%; average: Py1a 0.02 ± 0.01 wt%, Py1b 0.01 ± 0.02 wt%) are also lower than those of Py2 (range: dl–0.21 wt%; average: Py2a 0.03 ± 0.04 wt%, Py2b 0.02 ± 0.01 wt%) (Fig. 6d). Similarly, the average contents of Ag in Py1 (range: dl–0.04 wt%; Py1a 0.01 ± 0.01 wt%, Py1b 0.01 ± 0.01wt%) are lower than those of Py2 (range: dl–0.052 wt%; Py2a 0.02 ± 0.01%, Py2b 0.02 ± 0.01 wt%). The contents of other trace metals (e.g., Zn and Pb) measured by EPMA are similar in Py1 and Py2.

Trace element compositions of pyrite analyzed by LA–ICP–MS

Twenty-seven trace and rare earth elements (Co, Ni, Cu, Zn, As, Se, Mo, Ag, Sb, Au, Tl, Bi, Pb, La, Ce, Pr, Nd, Sm, Eu, Gd, Tb, Dy, Ho, Er, Tm, Yb, and Lu) were measured by LA–ICP–MS (ESM 2 Table 2). Although none of these elements show a systematic change in content from Py1a to Py2b, some are distinct (Figs. 7 and 8).

The gold contents of Py1 range from 0.003 to 82.4 ppm, and the average gold content increases significantly from 0.06 ppm in Py1a to 9.3 ppm in Py1b (Fig. 7a–e). The As contents of Py1 range from 1.93 to 1031 ppm, and the average As content shows no regular trend between Py1a (66.4 ppm) and Py1b (27.6 ppm) (Fig. 7h). However, the average gold contents of Py2 increase from 1.1 ppm in Py2a to 473.4 ppm in Py2b, higher than those in Py1 (0.1 to 10.0 ppm) (Fig. 7a–e).

The trace element compositions of Py1 and Py2 exhibit both similarities and differences. Specifically, they have similar Zn, Sb, and Tl contents, although Py1b and Py2b have relatively higher concentrations of Au and Ag than Py1a and Py2a (Figs. 7b, 9). Py2 is commonly enriched in chalcophile elements as shown by average concentrations of Ni (85.6 ppm), Cu (446.3 ppm), Se (100.1 ppm),

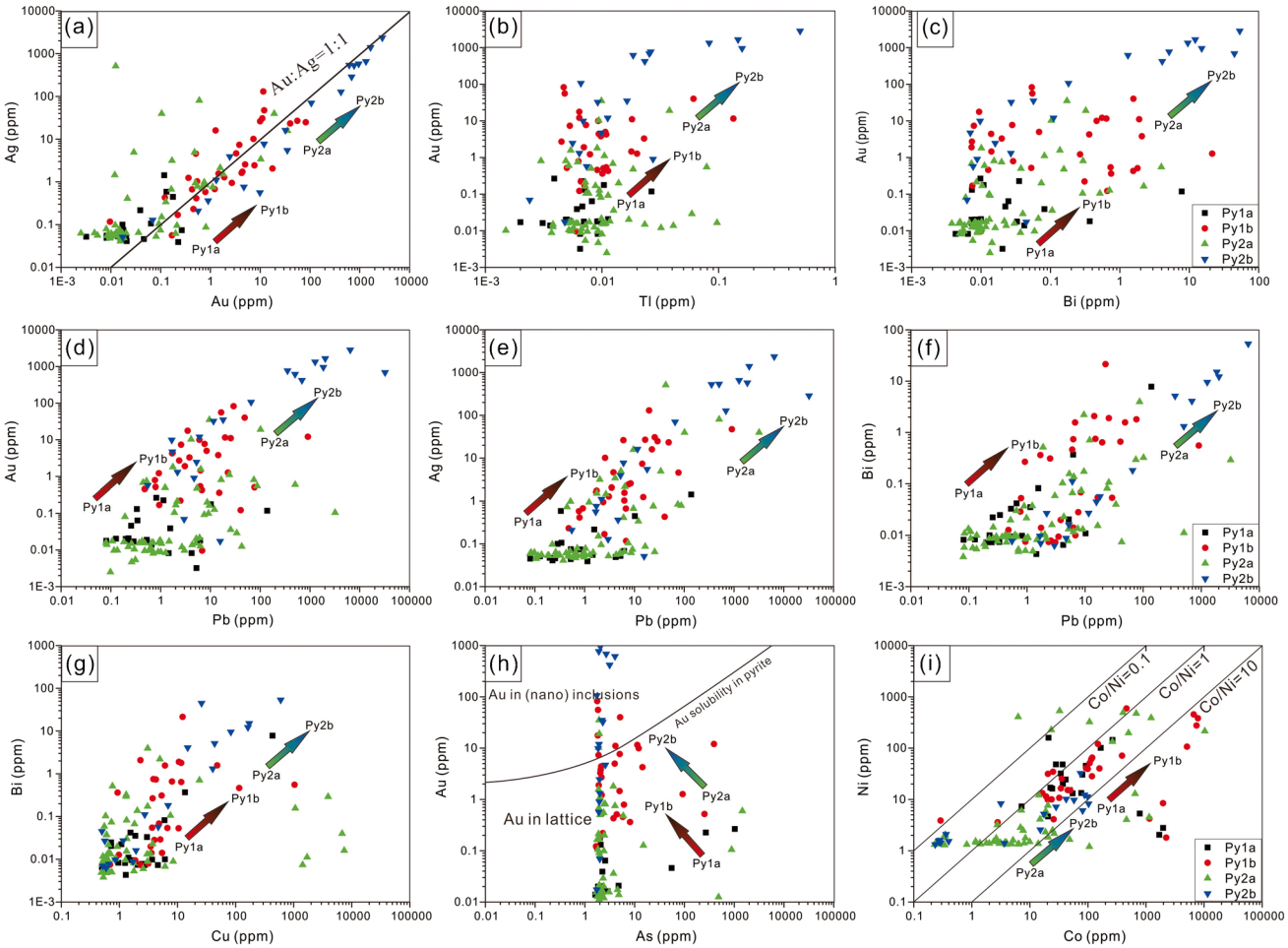

Fig. 7 Trace element compositions of pyrite analyzed by using LA–ICP–MS. **a** Ag–Au plot shows a trend of increasing Ag and Au contents from Py1a to Py2b. Most Py1a and Py2a plot in the Au/Ag < 1 field, whereas Py2b plots in the Au/Ag > 1 field; **b** Au–Tl plot shows a positive correlation; **c** Au–Bi plot shows a positive correlation. Py2b has the highest Au contents among the four types of pyrite; **d**, **e** Au–Pb and Ag–Pb plots show positive correlations; (**f**) Pb–Bi plot indicates that Py2a and Py2b have higher Bi and Pb contents than Py1a and Py1b; (**g**) Cu–Bi plot of the four types of pyrite; (**h**) Au–As plot shows no correlation; (**i**) Ni–Co plot shows that Py2a and Py2b plot mainly below, and Py1a and Py1b plot mainly above, the Co/Ni = 1 line

Mo (17.9 ppm), Ag (158.9 ppm), Pb (592.6 ppm), and Bi (2.88 ppm), whereas these elements have lower average concentrations in Py1: Ni (63.9 ppm), Cu (35.9 ppm), Se (23.0 ppm), Mo (0.26 ppm), Ag (9.4 ppm), Pb (28.7 ppm), and Bi (1.13 ppm) (Fig. 7c–g). However, the average contents of Co (783.2 ppm) and Zn (7.0 ppm) in Py1 are higher than those in Py2 (Co: 247.3 ppm; Zn: 4.6 ppm) (Fig. 7i). The remaining trace elements were not compared because of their low concentrations and limited variation.

The REE contents for Py1a, Py1b, Py2a, and Py2b are given in ESM 2 Table 3, and chondrite-normalized REE patterns are shown in Fig. 8. The REE patterns are generally similar but also show some differences. Py1a and Py1b have average $(La/Yb)_N$ values of < 0.28 and < 0.25, respectively. Py1b has a wider range of total REEs than Py1a (Fig. 8a; ESM 2 Table 3). The HREE distribution shows an obvious interelemental fractionation pattern. A pronounced positive Eu anomaly can be seen, and average Eu/Eu* values of Py1a and Py1b are < 1.16 and < 1.20, respectively. In addition, their average Ce/Ce* values are < 0.45 and < 0.49 for Py1a and Py1b, respectively. In contrast, Py2a and Py2b have relatively higher ΣREE and are HREE-enriched (Fig. 8b). The $(La/Yb)_N$ values of Py2a (< 0.38) and Py2b (0.55) are different, and their average Eu/Eu* values are also variable (Py2a: < 1.33; Py2b: 1.04), but their average Ce/Ce* values (Py2a: < 0.51; Py2b: < 0.55) are similar.

In-situ S isotope compositions of pyrite

Pyrite from nine representative samples was selected for S isotope analysis by LA–MC–ICP–MS (ESM 2 Table 4; Fig. 10). Each type of pyrite has a distinct range of S

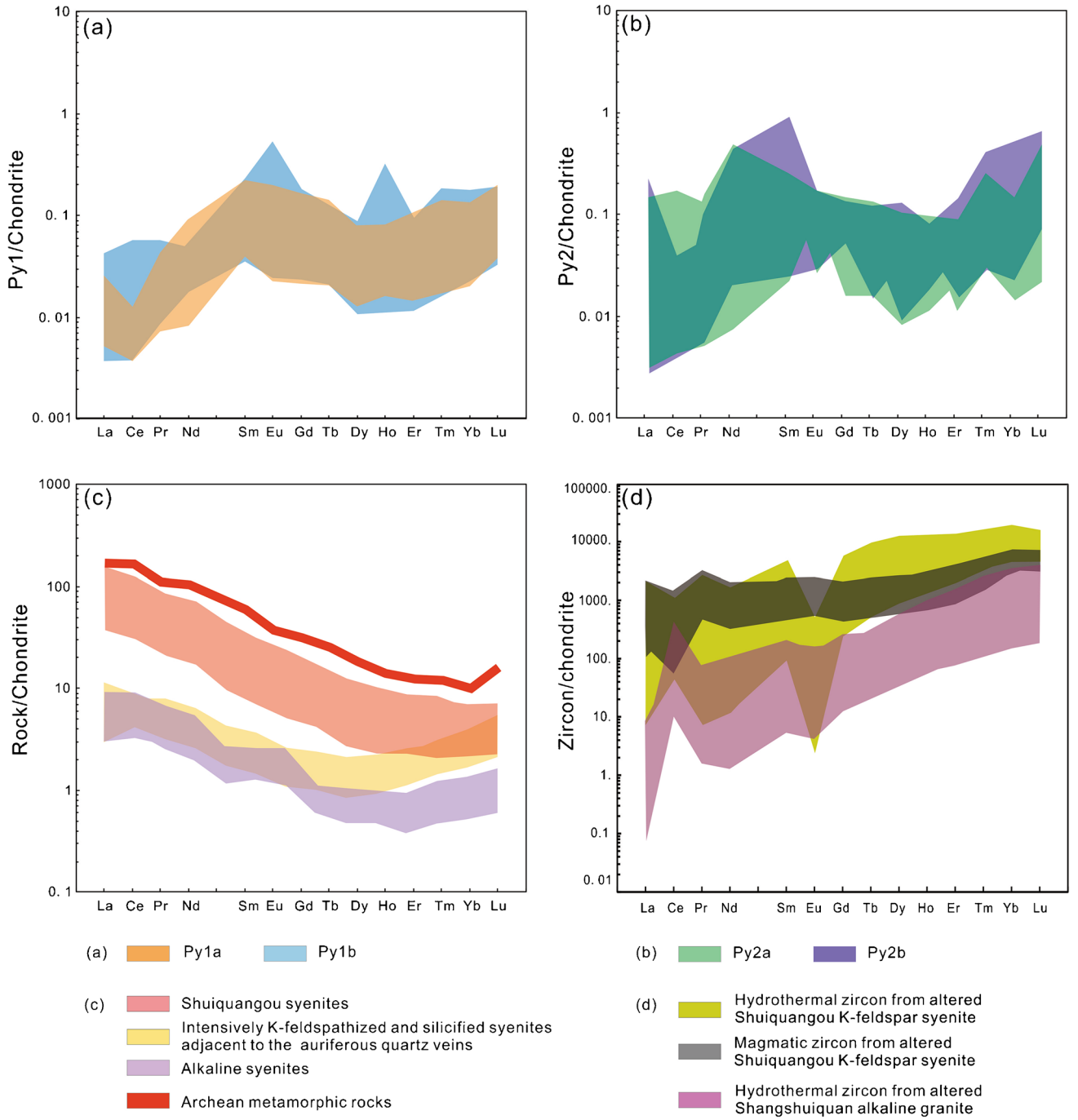

Fig. 8 Chondrite-normalized REE patterns of Dongping gold deposit samples: **a** Py1a and Py1b; **b** Py2a and Py2b; **c** Shuiquangou syenite, altered syenite adjacent to auriferous quartz veins, and Archean country rocks (data from Bao et al. 1996; Bao and Zhao 2003; Zhao et al. 2010); **d** hydrothermal and magmatic zircons from Shuiquangou syenite and Shangshuiquan granite (data from Li et al. 2018a). REE normalization values are from Sun and McDonough (1989)

isotope compositions. The average $\delta^{34}S$ values of Py1a (4 spots, $-4.3 \pm 0.5‰$) and Py1b (4 spots, $-4.9 \pm 1.6‰$) are higher than those of Py2a (12 spots, $-7.0 \pm 0.2‰$) and Py2b (4 spots, $-6.4 \pm 0.5‰$).

In-situ Pb isotope composition of pyrite

The Pb isotope composition of pyrite is given in ESM 2 Table 5 and shown in Fig. 11. Py1 is characterized by

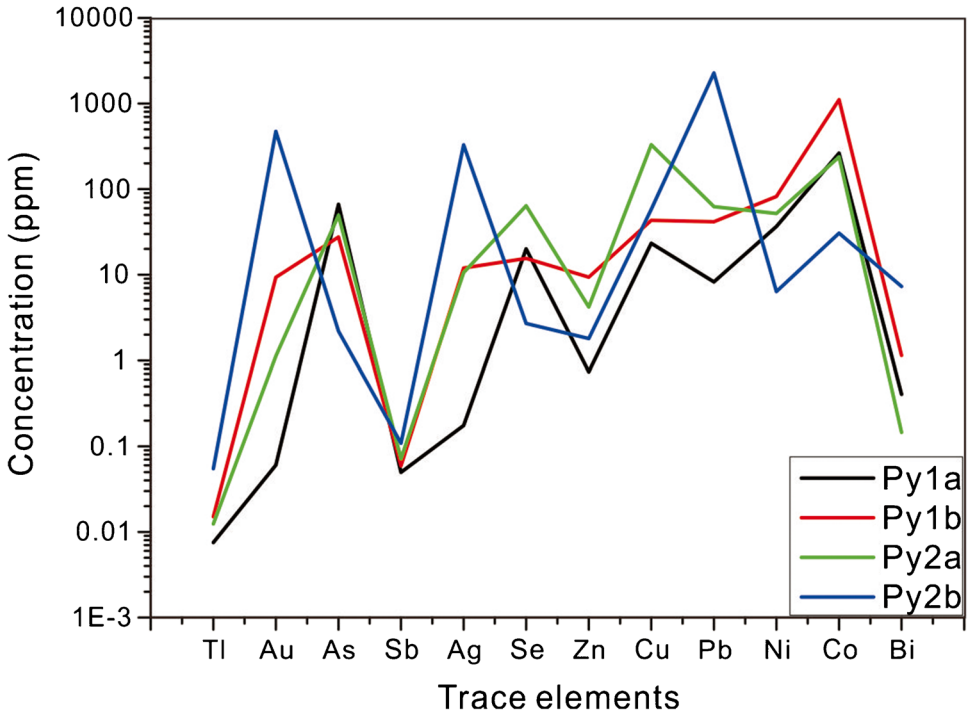

Fig. 9 Spider diagram illustrating trace element compositions of Py1a, Py1b, Py2a, and Py2b

narrow ranges of $^{206}Pb/^{204}Pb$ (17.38–17.58), $^{207}Pb/^{204}Pb$ (15.43–15.50), and $^{208}Pb/^{204}Pb$ values (37.30–37.58). Py2 has higher $^{206}Pb/^{204}Pb$ (17.52–17.83) and $^{208}Pb/^{204}Pb$ values (37.51–37.71) and almost identical $^{207}Pb/^{204}Pb$ values (15.47–15.57).

Discussion

Origin of hydrothermal fluids

The concentrations and ratios of trace elements (e.g., Co, Ni, and Se) in pyrite have been used to assess the origin of hydrothermal fluids (Huston et al. 1995; Belousov et al. 2016). For example, Co/Ni ratios are widely used to assess the origin of pyrite and to elucidate the genesis of hydrothermal ore deposits (Bajwah et al. 1987; Li et al. 2014a, b). Pyrite with Co/Ni ratios < 1 are generally considered to have a sedimentary origin, whereas pyrite with Co/Ni ratios > 1 (particularly between 1 and 5) are regarded as of hydrothermal origin (Loftus-Hills and Solomon 1967; Large et al. 2014). In some cases, hydrothermal pyrite may have Co/Ni ratios of < 1, in which case it is necessary to consider geological evidence such as the mineralogical characteristics and genetic type of the ore deposit (Bralia et al. 1979). Excluding abnormally high values caused by micro-inclusions, the Co/Ni ratios of Py1 and Py2 are 0.05−47.47 (average = 4.37) and 0.02−73.67 (average = 12.43), respectively (ESM 2 Table 2). The Co/Ni ratios of most pyrite are between 1 and 10 (Fig. 7i), indicating that pyrite precipitated from hydrothermal fluids. We speculate that hydrothermal fluids provided the ore-forming materials during both the early and late mineralization stages.

The Se contents of the four pyrite types vary considerably from those of Carlin-type to those of porphyry Cu-Au deposits (Keith et al. 2018). The Se contents in most pyrite range from a few to several dozens of ppm, whereas Py2a grains in sample DP23-3 possess the highest Se contents, ranging from 528 to 1657 ppm (ESM 2 Table 2). At the Bendigo orogenic gold deposit, the average Se contents of diagenetic and hydrothermal pyrite are 67 ppm and 32 ppm, respectively (Thomas et al. 2011). The Se-rich (mean = 319 ppm) hydrothermal pyrite of some Au deposits is thought to result from leaching of sedimentary rocks and transport by metamorphic fluids (Brill 1989). The high Se contents of the late-stage pyrite at Dongping indicate that sedimentary Se participated in the Au mineralization process.

In hydrothermal systems, rare earth elements (REEs) can be used to trace the source of hydrothermal fluids and the degree of water–rock interaction (Henderson 1984; Wang et al. 2012; Li et al. 2018b). The ΣREEs of pyrite from the Dongping gold deposit are low but increase progressively from Py1a to Py2b (Fig. 8a, b). The chondrite-normalized REE patterns of early- and late-stage pyrite are different from those of the Archean country rocks and intensely altered syenite adjacent to the auriferous quartz veins (Fig. 8a–c), which suggests that the pyrite REEs were derived from another source. Both early- and late-stage pyrites are relatively HREE-enriched, possibly due to discrimination against LREEs in the pyrite crystal lattice (Fan et al. 2000; Li et al.

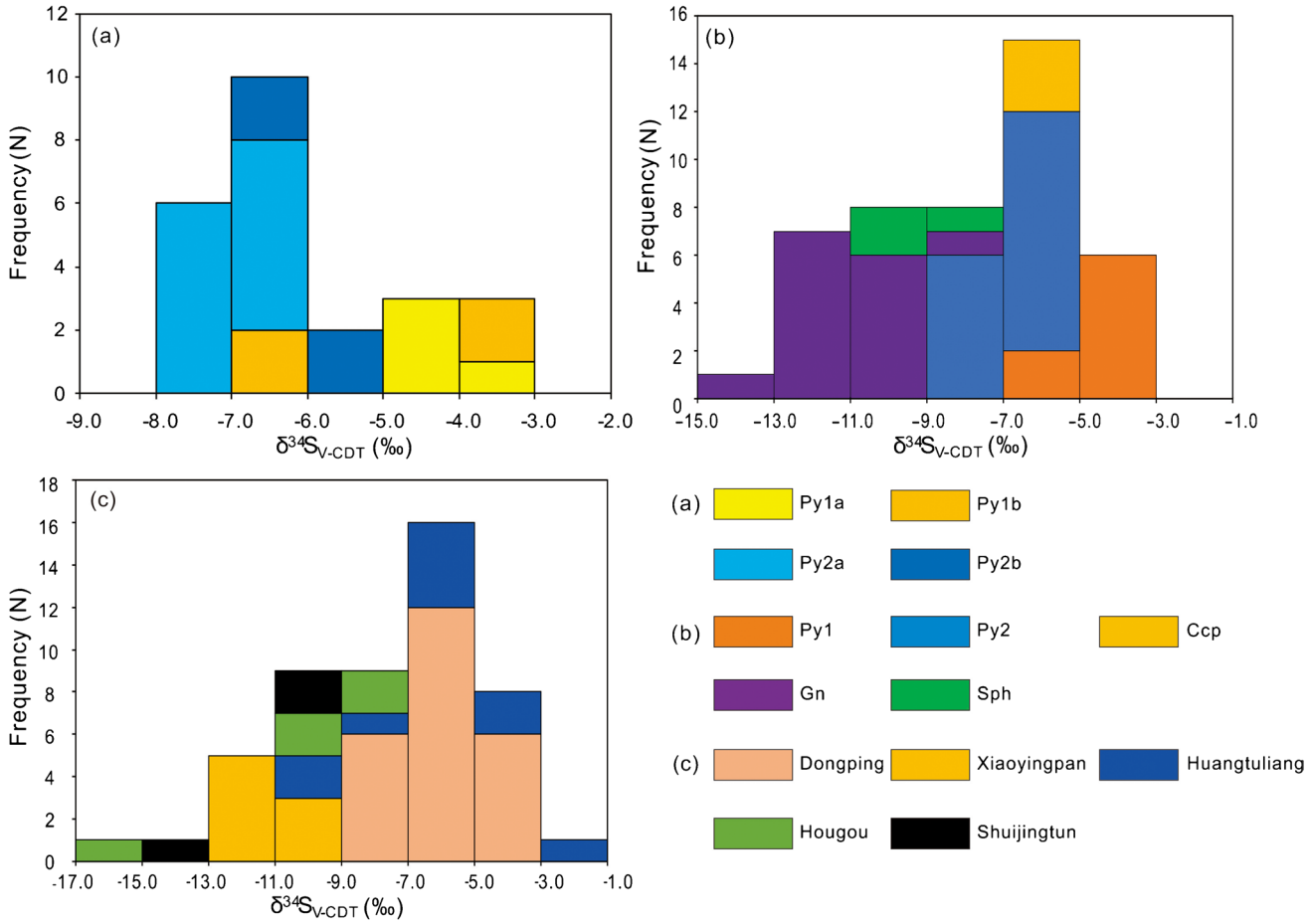

Fig. 10 Histograms of sulfur isotope compositions of **a** four types of pyrite in the Dongping gold deposit; **b** sulfide minerals in the Dongping gold deposit; **c** pyrite from the Dongping, Xiaoyingpan, Huangtuliang, Hougou, and Shuijingtun gold deposits hosted by the Shuiquangou syenite complex. Data are from this study and Wang et al. (1990), Yin (1994), Song and Zhao (1996), Nie (1998), Li et al. (2000), Xing et al. (2011), and Bao et al. (2016)

2003; Wang et al. 2004), whereas the syenite and Archean country rocks are LREE-enriched. Moreover, the Ce and Eu anomalies of Py1a and Py1b are similar to those of magmatic and hydrothermal zircons in the Shuiquangou syenite (Fig. 8a, d), whereas those of Py2a are similar to those of hydrothermal zircons in the Shangshuiquan granite (Fig. 8b, d). These observations may indicate a close genetic relationship between Py1 and the Shuiquangou syenite, as well as between Py2 and the Shangshuiquan granite.

Sulfur isotope compositions are commonly useful tools for defining both the source and genesis of sulfides (Ohmoto and Rye 1979; Ulrich et al. 2011; Li et al. 2013; Zhang et al. 2014; Laflamme et al. 2018; Zhai et al. 2018). The $\delta^{34}S$ values of Py1a and Py1b (−4.3‰ and −5.0‰, respectively) are ~2‰ higher than those of Py2a and Py2b (−7.0‰ and −6.4‰, respectively), suggesting that S sources changed during each mineralization stage. Negative $\delta^{34}S$ values in sulfides can be interpreted as indicating a biogenic or sedimentary sulfur source, or the incorporation of oxidized magmatic fluids, or isotopic fractionation during the evolution of the mineralizing fluid (Ohmoto and Rye 1979; Phillips et al. 1986; Cameron and Hattori 1987; Oberthuer et al. 1996; Hodkiewicz et al. 2009). For both Py2a and Py2b, S isotope compositions are heterogeneous within single grains, as shown by systematically higher $\delta^{34}S$ values in the core of a grain relative to its rim (ESM 2 Table 4). Song and Zhao (1996) measured the S isotopic compositions of co-occurring pyrite, sphalerite, and galena at Dongping, yielding similar negative $\delta^{34}S$ values for all mineral phases. Total S isotopic compositions for the early mineralization stage were calculated using equations from Ohmoto and Rye (1979), yielding estimates ranging from −1 to +2‰. This result is similar to the S-isotopic compositions of pyrite in the Shuiquangou syenite ($\delta^{34}S$ = +1.8 to +3‰; Nie 1998; Bao et al. 2016). We speculate that the Shuiquangou syenite provided sulfur and perhaps metals during the early stage of mineralization at Dongping. The $\delta^{34}S$ values of pyrite from regional gold deposits hosted in the Shuiquangou syenite

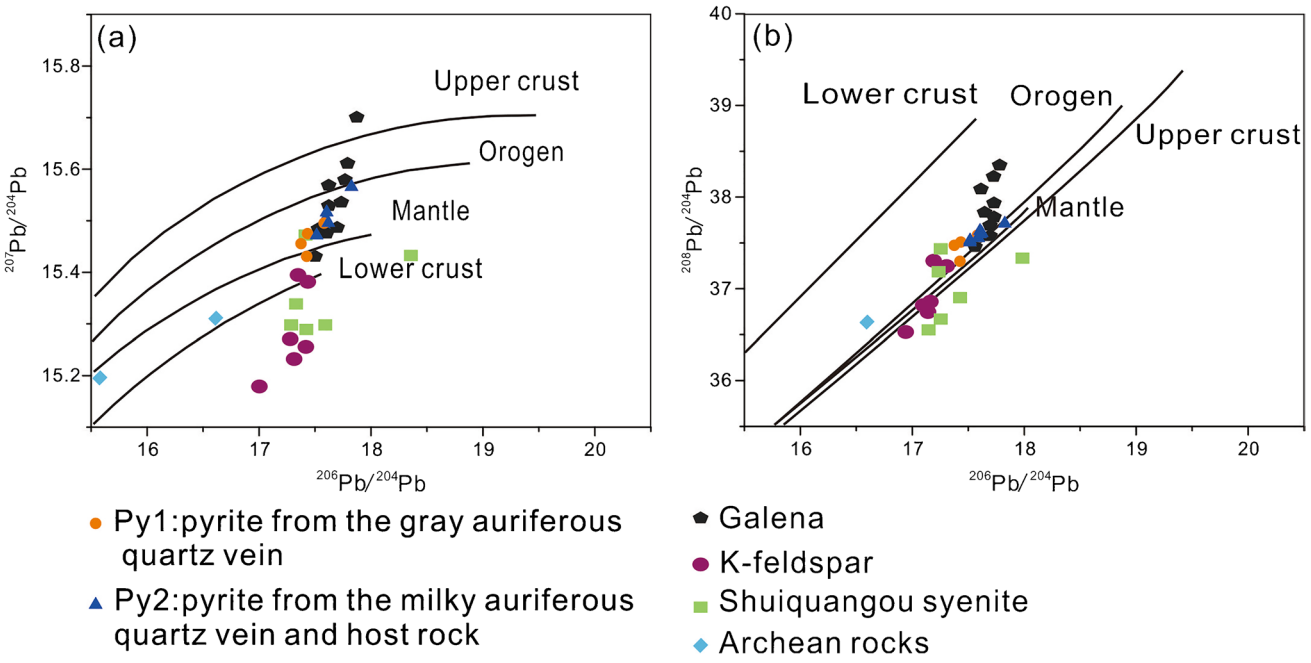

Fig. 11 Lead isotope compositions of Py1 and Py2, galena, K-feldspar, syenite, and Archean rocks in the Dongping gold deposit. **a** $^{207}Pb/^{204}Pb$ vs. $^{206}Pb/^{204}Pb$; **b** $^{208}Pb/^{204}Pb$ vs. $^{206}Pb/^{204}Pb$. Data are from this study and Nie (1998) and Bao et al. (2016). The evolution curves are from Zartman and Haines (1988)

are all negative values (− 17 to − 1; Fig. 10c; Song and Zhao 1996; Nie 1998; Li et al. 2000; Bao et al. 2016), which indicates that the Shuiquangou syenite may have provided sulfur to these deposits. Compared with Py1, the $\delta^{34}S$ values of Py2 are more negative (down to − 7), indicating a different sulfur source may have involved in this stage, e.g., metamorphic rocks. Previous studies have shown that the Precambrian metasedimentary rocks of the North China Craton are enriched in isotopically light sulfur (^{32}S) (Jo et al. 2021; Liu et al. 2022). Thus, we suggest that early-stage hydrothermal fluids in the Dongping gold deposit were derived mainly from the Shuiquangou syenite, and late-stage ore-forming materials mainly from the Shangshuiquan granite with a larger contribution from Archean metamorphic rocks.

Our Pb isotope compositions of pyrite (ESM 2 Table 5; Fig. 11) were combined with previous Pb isotopic data from the Dongping gold deposit (Nie 1998; Fan et al. 2001; Bao and Zhao 2006; Bao et al. 2016) to evaluate Pb sources. Py1 has lower isotopic ratios and therefore contains less radiogenic Pb than Py2. On a $^{207}Pb/^{204}Pb$ versus $^{206}Pb/^{204}Pb$ diagram (Fig. 11a), Py2 and Py1 generally plot between the mantle and orogenic reservoir compositions, although Py1 also plots between the lower continental crust and mantle reservoir compositions. We infer that early-stage ore fluids obtained Pb from both the lower crust and mantle, whereas late-stage fluids derived more radiogenic Pb mainly from the lower crust. On a $^{208}Pb/^{204}Pb$ vs. $^{206}Pb/^{204}Pb$ diagram (Fig. 11b), most samples plot between the mantle and lower crust lines, indicating multiple sources of Pb. Previous studies reported that sulfides, disseminated ores, and auriferous quartz veins plot along an array defined by the Pb isotope compositions of K-feldspar, syenite, and Archean metasedimentary rocks, which is indicative of mixing between two Pb sources (Nie 1998; Bao et al. 2000, 2016). Moreover, Py1 and the Shuiquangou syenite have similar Pb isotopic compositions (Fig. 11a, b), which suggests that the syenite provided Pb and perhaps other metals to hydrothermal fluids during early-stage mineralization. In contrast, Py2 has a greater radiogenic Pb content than Py1, indicating that the Shuiquangou syenite was not involved in late-stage mineralization, and that a radiogenic source of Pb was involved. We surmise that the Shangshuiquan granite was the major source of Pb during late-stage mineralization, and that the Pb contribution from Archean rocks became more significant. The Shuiquangou syenite was produced by fractional crystallization of mantle-derived melts (Li et al. 2018a), whereas the Shangshuiquan granite was derived from the lower continental crust by partial melting (Jiang et al. 2009), making the latter a likelier source of radiogenic Pb.

Fluid evolution during the two mineralization stages

Siderophile and chalcophile elements (e.g., Co, Ni, As, Se, and Te) are commonly accommodated in pyrite via substitution for Fe (Zhang et al. 2014). However, EPMA results

(Fig. 6a, c, d) reveal that Fe shows no correlation with any of these elements. The low trace element contents of Py1a and Py2a may have been due to rapid pyrite growth rates, causing weak adsorption of cations from solution onto the growing crystal surfaces.

The REE composition of pyrite is controlled not only by its crystal texture but also by the REE characteristics of the hydrothermal fluid (Yuan et al. 2017). Differences in the ionic radii of REE^{3+} and Fe^{2+} make accommodation of REEs in Fe structural sites of the pyrite lattice difficult (Mao et al. 2009), and thus REEs tend to build up in fluid inclusions (Li et al. 2003; Fan et al. 2000; Wang et al. 2004; Shannon 1976; Mao et al. 2009). In the Dongping gold deposit, Py2a and Py2b have higher ΣREE contents than Py1a and Py1b. The high ΣREE contents of Py2a may have been caused by release of REEs from HREE-rich inclusions. In addition, water–rock interaction may have played a role in uptake and transport of REEs, particularly the HREEs, which preferentially enter into solution relative to the LREEs (Mao et al. 2009). The more variable and higher REE contents of Py2 relative to Py1 suggest intense fluid interaction of the pyrite with the Shangshuiquan granite and Archean metamorphic rocks. In addition, some Py1a grains show an obvious positive Ce anomaly due to formation in an oxidizing environment (Fig. 8b; Li et al. 2014a, b; Kong et al. 2016).

The more negative $\delta^{34}S$ values of Stage-2 pyrite likely resulted from sulfur isotope fractionation in a high-fO_2 hydrothermal fluid (Zhang et al. 2022). Fluid oxidation is evidenced by a general decreasing trend of $\delta^{34}S$ values from the parent euhedral pyrite to porous pyrite (Fig. 10). Dissolution of the parent pyrite and precipitation of the later pyrite may have occurred at low pH in an Fe^{2+}-rich fluid caused by partial oxidation of aqueous H_2S and/or S^{2-} in ore fluids (Wu et al. 2019).

Textural and chemical differences among the multiple generations of pyrite allow the migration of gold and other metals to be tracked throughout the formation process of gold deposits (Large et al. 2009). Py1a and Py1b are enriched in Co, Zn, and S and contain only minor Au and As (ESM 2 Table 2), which indicates that early-stage hydrothermal fluids were Au-poor and contributed relatively little to ore formation. In contrast, Py2a and Py2b are strongly enriched in Au and As and moderately enriched in Ag, Tl, Bi, and Pb (Fig. 8), which indicates that Au-As transport and deposition occurred during late-stage mineralization (Cook et al. 2009; Large et al. 2009, 2013). During the replacement of euhedral pyrite, depletion of gold and other trace elements in porous pyrites (Py1b and Py2b) relative to their precursors (Py1a and Py2a) indicates remobilization of these metals from the crystal lattice of the original pyrite (Fig. 5d, i; Wu et al. 2019). The variable but in general more radiogenic Pb isotope ratios in late, porous, and inclusion-rich pyrite (Py2b) can be attributed to modification of and precipitation from a highly evolved crustal fluid during the re-precipitation of native gold (Ma et al. 2022).

In summary, the trace element redistribution sequence during precipitation of Py1a, Py1b, Py2a, and Py2b plus or minus associated sulfides can be described as follows: (1) Py1a + fluids (Tl^+, Au^+, Ag^+, Zn^{2+}, Cu^{2+}, Pb^{2+}, Ni^{2+}, Co^{2+}, Bi^{2+})$_{(aq)}$ → Py1b + fluids (As^{2+}, Se^{2+})$_{(aq)}$ and (2) Py2a + Ccp + Gn + Sp + fluids (Tl^+, Au^+, Ag^+, Pb^{2+}, Bi^{2+}, Sb)$_{(aq)}$ → Py2b + fluids (As^{2+}, Se^{2+}, Zn^{2+}, Cu^{2+}, Ni^{2+}, Co^{2+})$_{(aq)}$.

Gold occurrence and precipitation

In the Dongping gold deposit, pyrite is the main host mineral of gold. Gold occurs within pyrite as lattice-substituted gold and in micro- to nanograins, in the form of native gold, electrum, or Au–Ag tellurides (Fig. 5g–h). Our LA–ICP–MS results show a systematic increase in the Au and trace element content from Py1 to Py2 (Fig. 7). Gold may occur in submicroscopic inclusions of discrete Au-bearing phases (Large et al. 2007, 2009, 2013; Cook et al. 2009; Fougerouse et al. 2016). Py2a and Py2b contain significant amounts of Au and Ag, e.g., spot analyses of Py2b reveal concentrations up to 1000–2000 ppm (Fig. 5i). However, there is no correlation between the Au and As contents, as seen in previous studies (e.g., Morishita et al. 2018).

The four types of pyrite have similar As contents, and most data plot below the "gold solubility in pyrite" line (Fig. 7h; Reich et al. 2005), although some analyses plot above the line, indicating that Au exists as nano-inclusions. We propose that most gold was incorporated into the pyrite lattice as Au^+, with a small fraction present as nanoparticles of native gold (Au^0) within cavities, pores, and interstices in Py2b (Fig. 5h, i; Simon et al. 1999; Reich et al. 2005).

The substitution of S for As in pyrite reduces the symmetry around the iron atom and results in structural distortion and formation of defects that can facilitate the incorporation of gold into pyrite (Simon et al. 1999; Reich et al. 2005; Deditius et al. 2014; Li et al. 2019). The positive correlations between Au and Ag, Ti, Pb, and Bi indicate that gold was co-precipitated with these elements in pyrite, perhaps as inclusions (Fig. 7a–e).

In the Dongping gold deposit, Cook et al. (2009) observed a good correspondence between high gold values and two key textural criteria: areas of clustered inclusions, and microshearing and fracturing/brecciation within pyrite grains. In this study, we found that porous Py1b has a higher Au content relative to Py1a (Fig. 5d). High Au contents have also been obtained from spots within porous Py2b grains (Fig. 5i). The enrichment of Au in the late-stage pyrite was a result of leaching of earlier-formed Au from microfractures during pyrite recrystallization (Fig. 5c, d, f, i) (Large et al. 2009; Bi et al. 2011; Velasquez et al. 2014).

The Shuiquangou syenite, Shangshuiquan granite, and Archean metamorphic rocks are all thought to contain substantial amounts of ore-forming materials. However, ore-forming metals, e.g., Au, As, Ag, Cu, Pb, and Zn, were not rich in early intrusive rocks and magmatic fluids (those forming Py1) but were remarkably enriched in later hydrothermal fluids (those forming Py2). The high gold content in Py2b suggests a contribution from magmatic-hydrothermal fluids derived from the contemporary Shangshuiquan granite, which may have also been circulated in the Archean metamorphic rocks. According to the S and Pb isotope data, ore-forming metals were derived in part from the mantle during the early mineralization stage, but mainly from the lower continental crustal and Archean metamorphic rocks during the late mineralization stage.

A two-stage mineralization model: pyrite perspective

The texture, structure, and trace element compositions of pyrite can provide evidence for overprinting of mineralization events and their differing impacts on Au distribution (Baker et al. 2006; Cook et al. 2009). The LA–ICP–MS data indicate that only minor Au was deposited from hydrothermal fluids in Py1a, whereas Py2b has the highest Au contents. The variable Co and Ni contents of pyrite support an origin from a magma-related hydrothermal system derived from multiple sources. Mineralization may have been related to the proximity of the Devonian Shuiquangou syenite complex and the Cretaceous Shangshuiquan granite, an inference that is consistent with the results of earlier studies. For instance, Nie (1998), Bao et al. (2016), and Nie et al. (2004) suggested that pyrite with positive $\delta^{34}S$ values was derived from the Shuiquangou syenite complex; and Cisse et al. (2017) and Miao et al. (2002) inferred that mineralization in the Dongping region was of magmatic hydrothermal origin, with a mixture of mafic magmas derived from the mantle and felsic magmas derived from partial melting of ancient Archean metamorphic rocks. The Shangshuiquan granite served as a potential source of ore-forming materials owing to its close relationship with the late-stage, milky colored, and gold-bearing quartz veins.

Based on our textural, mineralogical, multi-element, and isotopic studies of pyrite as well as the results of previous research (Nie 1998; Miao et al. 2002; Cook et al. 2009; Bao et al. 2016; Cisse et al. 2017; Li et al. 2018a), we propose that the Dongping gold deposit was the result of two episodes of mineralization (Fig. 12), with most of the gold emplaced during Stage 2.

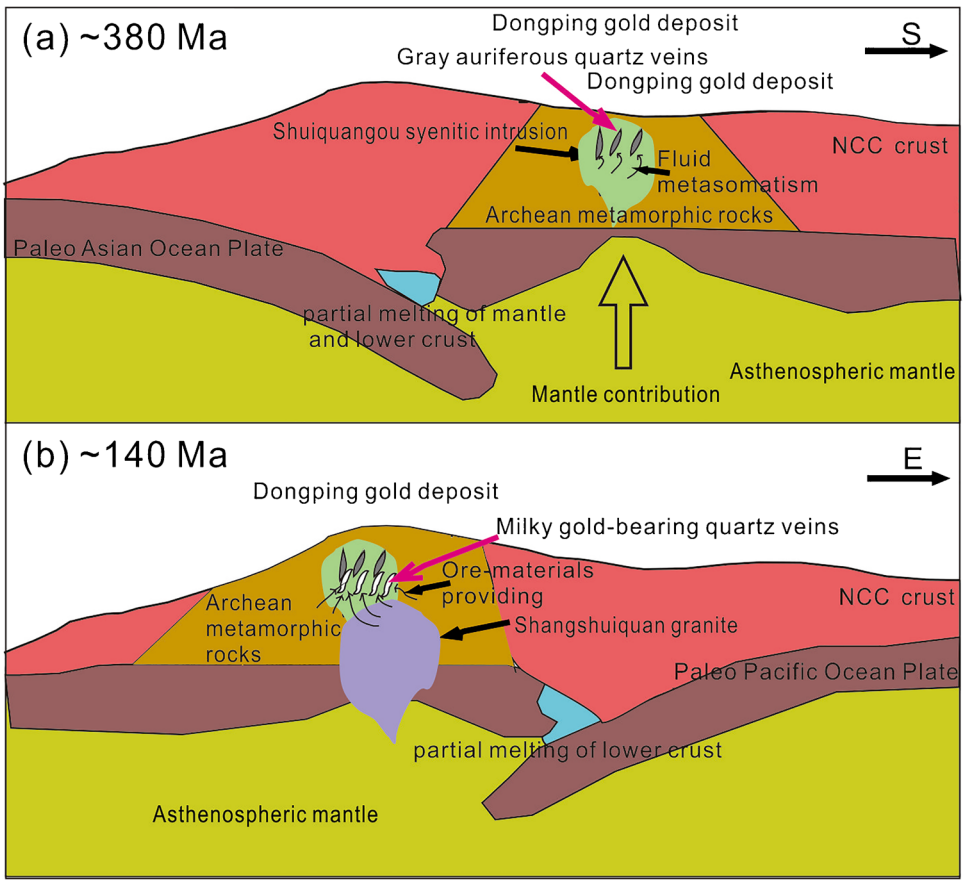

Fig. 12 Schematic diagrams illustrating the two stages of gold mineralization in the Dongping gold deposit. **a** Early-stage mineralization was associated mainly with intrusion of Devonian Shuiquangou syenite generated by Paleozoic subduction of the paleo-Asian Ocean Plate beneath the North China Craton; **b** late-stage mineralization was related to emplacement of the Cretaceous Shangshuiquan granite generated by Mesozoic subduction of the paleo-Pacific Plate beneath the North China Craton, with significant contributions from Archean metamorphic rocks

The first stage of mineralization, which occurred during the Devonian (~ 380 Ma), was related to intrusion of the Shuiquangou syenite generated by Paleozoic subduction of the paleo-Asian Ocean Plate beneath the North China Craton (Fig. 12a, Zhang et al. 2010). During post-collision extension, mantle-derived magma melted pre-existing lower continental crust, forming a mixed magma for the Shuiquangou syenite (Shao et al. 1999; She et al. 2006; Chen et al. 2008; Zhang et al. 2009). The gray-colored, auriferous quartz veins in the Dongping gold deposit formed after emplacement of the Shuiquangou syenite. The hydrothermal fluids derived from syenite intrusions had high F and K contents (Fan et al. 2001; Gao et al. 2015, 2017; Wang et al. 2019a) and resulted in strong potassic metasomatism (Figs. 4e, 5b, c). Gold derived from the syenite may have been transported as sulfide and/or telluride complexes in the hydrothermal fluids (Bao et al. 2016). The cooling caused by extensive silicification and potassic metasomatism contributed to the precipitation of gold.

The second stage of mineralization was related to emplacement of the Cretaceous (~ 140 Ma) Shangshuiquan granite, which was generated by subduction of the paleo-Pacific Plate beneath the North China Craton (Fig. 12b; Li et al. 2018a). The Shangshuiquan granite originated from partial melting of the ancient lower continental crust (Ma et al. 2012), and its parent magma may have been I-type and experienced extensive fractional crystallization (Jiang et al. 2009). Lithospheric thinning accompanied by asthenospheric upwelling and lower crustal degassing produced large amounts of magma that provided abundant fluids and heat for gold mineralization (Mao et al. 2008; Li et al. 2012a, b, c; Li et al. 2018a). Fluids exsolved from the Shangshuiquan granite leached S and Pb from Archean metamorphic rocks. Hydrothermal fluids migrating along faults and fissures in Archean basement rocks were the main source of late-stage gold deposited during the Cretaceous.

Applicability to other gold deposits

The northern margin of the North China Craton is well-known for gold deposits, with reserves of about 900 tons of gold. The gold district occurs as an E-W-trending belt (~ 1500 km long) in which metamorphosed Archean and Proterozoic strata were episodically uplifted during Paleozoic and Mesozoic deformation events. Most gold deposits are hosted by uplifted Precambrian metamorphic rocks, and ~ 30% of the deposits are hosted by Paleozoic and Mesozoic syenite and granite (Qiu et al. 1993; Nie 1997; Deng et al. 2014; Fu et al. 2020). The gold deposits in the northern NCC, such as Dongping, possess common features to other intrusion-related gold deposits worldwide: (1) spatial and temporal associations with igneous rocks; (2) high Au/Ag ratios and anomalous Te contents; and (3) CO_2-rich ore fluids associated with the degassing of alkalic igneous rocks (Mutschler et al. 1985; Thompson et al. 1985; Richards and Kerrich 1993; Helt et al. 2014; Bao et al. 2016). Richards and Kerrich (1993) suggested that the ore-forming materials of these deposits were remobilized from early crystallized granitic bodies, whereas other studies inferred that the metals may have come directly from magmas (Werle et al. 1984; Anderson et al. 1987). With regard to the "Dongping-type" gold deposits on the northern margin of the NCC, these possible genetic associations deserve further study.

The multistage mineralization events of the gold deposits on the northern margin of the NCC are consistent with episodic tectonic activation and associated magmatism. Four major magmatic episodes have been recognized on the northern margin of the NCC: Devonian (390–353 Ma), Triassic (236–218 Ma), Jurassic (199–161 Ma), and Cretaceous (143–125 Ma) (Deng and Wang 2016). The Devonian magmatic episode, represented by the Shuiquangou syenite and the Dahuabei granite in the study region, was related to arc accretion. The Triassic magmatic episode, represented by some monzogranite and igneous dikes, was a post-collisional event following closure of the Central Paleo-Asian Ocean. The Jurassic magmatic episode, represented by granite and quartz diorite, may represent the post-orogenic stage. The Cretaceous event, represented by the Shangshuiquan granite at Dongping, has been related to lithospheric thinning, coinciding with widespread Cretaceous magmatic activity in eastern China (Miao et al. 2002; Deng et al. 2004, 2009). Recent geochronological studies of these deposits support a multi-stage mineralization process, ranging from the Devonian to the Cretaceous (Zhang et al. 2013; Deng et al. 2014; Gao et al. 2014; Jia et al. 2018; Fu et al. 2020).

In summary, we propose that gold deposits on the northern margin of the NCC underwent multistage mineralization events, and that Cretaceous hydrothermal fluids had the largest influence on formation of large-scale gold deposits. Therefore, regional gold exploration may need to pay more attention to late-stage superposition of gold in mineralized deposits. The Cretaceous magmatic episode may have directly enhanced the ore-forming process and contributed large amounts of ore to these gold deposits, which should be regarded as the most favorable prospecting direction in the region.

Conclusions

1. Two stages of gold mineralization in the Dongping gold deposit have been differentiated based on pyrite texture and geochemistry. Early-stage hydrothermal fluids were mainly derived from the Devonian Shuiquangou syenite with a larger mantle contribution, whereas late-stage hydrothermal fluids were mainly derived from the Cretaceous

Shangshuiquan granite with significant material input from Archean Sanggan Group metamorphic rocks.

2. The trace element redistribution process during precipitation of Py1a, Py1b, Py2a, and Py2b plus or minus associated sulfides can be described as follows: (1) Py1a + fluids (Tl^+, Au^+, Ag^+, Zn^{2+}, Cu^{2+}, Pb^{2+}, Ni^{2+}, Co^{2+}, Bi^{2+})$_{(aq)}$ → Py1b + fluids (As^{2+}, Se^{2+})$_{(aq)}$ and (2) Py2a + Ccp + Gn + Sp + fluids (Tl^+, Au^+, Ag^+, Pb^{2+}, Bi^{2+}, Sb)$_{(aq)}$ → Py2b + fluids (As^{2+}, Se^{2+}, Zn^{2+}, Cu^{2+}, Ni^{2+}, Co^{2+})$_{(aq)}$.

3. Gold occurs as macroscopic native gold and microscopic gold in solid solution and within the crystal lattice of pyrite. High Au contents occur mainly in the rims, fractures, and pores of Stage-2 pyrite grains. The enrichment of Au in the late-stage pyrite was a result of leaching of earlier-formed microscopic Au from microfractures during pyrite recrystallization.

Supplementary Information The online version contains supplementary material available at https://doi.org/10.1007/s00126-022-01128-w.

Acknowledgements We thank two anonymous referees, David Dolejs (Associate Editor) and Georges Beaudoin (Editor-in-Chief), for their valuable comments that significantly improved the paper.

Funding This study was supported by the National Key Research and Development Plan (Fund number: 2016YFC0600104).

Declarations

Competing interests The authors declare no competing interests.

References

Anderson WB, Antonio M, Davis B, Jones GFP, Setterfield TN, Tua P (1987) The Emperor epithermal gold deposit, Vatukoula, Fiji. in The geology, structure, mineralization and economics of the Pacific Rim (Australian Institute of Mining and Metallurgy, ed.), 9–12, Proceedings of Pacific Rim Congress 1987

Bajwah ZU, Seccombe PK, Offler R (1987) Trace-element distribution Co: Ni ratios and genesis of the Big Cadia iron-copper deposit, New South Wales, Australia. Miner Deposita 22:292–300

Baker T, Mustard R, Brown V, Pearson N, Stanley CR, Radford NW, Butler I (2006) Textural and chemical zonation of pyrite at Pajingo: a potential vector to epithermal gold veins. Geochem-Explor Env A 6:283–293

Bao ZW, Zhao ZH (2003) Rare-earth element mobility during ore-forming hydrothermal alteration: a case study of Dongping gold deposit, Hebei province, China. Chin J Geochem 22:45–57

Bao ZW, Zhao ZH (2006) Isotopic geochemical constrains on metallogeny of the Dongping-type gold deposits associated with syenite. Acta Petrol Sin 22:2534–2542

Bao ZW, Zhao ZH, Zhou LD, Zhou GF (1996) An investigation into the petrogenesis of the Shuiquangou syenite complex, northwest of Hebei province. Acta Petrol Sin 12:562–572 (in Chinese with English abstract)

Bao ZW, Zhao Z, Zhang P, Wang YJG (2000) Lead isotopic compositions of the Dongping-type gold deposit and their exploration application. Geochimica 29:223–230 (in Chinese with English abstract)

Bao ZW, Sun W, Li C, Zhao Z (2014) U-Pb dating of hydrothermal zircon from the Dongping gold deposit in North China: constraints on the mineralization processes. Ore Geol Rev 61:107–119

Bao ZW, Li CJ, Zhao ZH (2016) Metallogeny of the syenite-related Dongping gold deposit in the northern part of the North China Craton: a review and synthesis. Ore Geol Rev 73:198–210

Barker SLL, Hickey KA, Cline JS, Dipple GM, Kilburn MR, Vaughan JR, Longo AA (2009) Uncloaking invisible gold: use of nanosims to evaluate gold, trace elements, and sulfur isotopes in pyrite from Carlin-type gold deposits. Econ Geol 104:897–904

Belousov I, Large RR, Meffre S, Danyushevsky LV, Steadman J, Beardsmore T (2016) Pyrite compositions from VHMS and orogenic Au deposits in the Yilgarn Craton, Western Australia: implications for gold and copper exploration. Ore Geol Rev 79:474–499

Bi SJ, Li JW, Zhou MF, Li ZK (2011) Gold distribution in As-deficient pyrite and telluride mineralogy of the Yangzhaiyu gold deposit, Xiaoqinling district, southern North China craton. Miner Deposita 46:925–941

Bralia A, Sabatini G, Troja F (1979) A revaluation of the Co/Ni ratio in pyrite as geochemical tool in ore genesis problems - evidences from southern tuscany pyritic deposits. Miner Deposita 14:353–374

Brill BA (1989) Trace-element contents and partitioning of elements in ore minerals from the CSA Cu-Pb-Zn deposit, Australia, and implications for ore genesis. Can Mineral 27:263–274

Cameron EM, Hattori K (1987) Archean gold mineralization and oxidized hydrothermal fluids. Econ Geol 82:1177–1191

Chen B, Tian W, Liu AK (2008) Petrogenesis of the Xiaozhangjiakou mafic–ultramafic complex, North Hebei: constraints from petrological, geochemical and Nd–Sr isotopic data. Geol J China Univ 14(3):295–303

Cisse M, Lu X, Algeo TJ, Cao XF, Li H, Wei M, Yuan Q, Chen M (2017) Geochronology and geochemical characteristics of the Dongping ore-bearing granite, North China: sources and implications for its tectonic setting. Ore Geol Rev 89:1091–1106

Cook NJ, Ciobanu CL, Mao JW (2009) Textural control on gold distribution in As-free pyrite from the Dongping, Huangtuliang and Hougou gold deposits, North China Craton (Hebei Province, China). Chem Geol 264:101–121

Cook NJ, Ciobanu CL, Meria D, Silcock D, Wade B (2013) Arsenopyrite-pyrite association in an orogenic gold ore: tracing mineralization history from textures and trace elements. Econ Geol 108:1273–1283

Deditius AP, Utsunomiya S, Ewing RC, Chryssoulis SL, Venter D, Kesler SE (2009) Decoupled geochemical behavior of As and Cu in hydrothermal systems. Geology 37:707–710

Deditius AP, Utsunomiya S, Reich M, Kesler SE, Ewing RC, Hough R, Walshe J (2011) Trace metal nanoparticles in pyrite. Ore Geol Rev 42:32–46

Deditius AP, Reich M, Kesler SE, Utsunomiya S, Chryssoulis SL, Walshe J, Ewing RC (2014) The coupled geochemistry of Au and As in pyrite from hydrothermal ore deposits. Geochim Cosmochim Acta 140:644–670

Deng J, Wang Q (2016) Gold mineralization in China: metallogenic provinces, deposit types and tectonic framework. Gondwana Res 36:219–274

Deng J, Yang LQ, Gao BF, Sun ZS, Guo CY, Wang QF, Wang JP (2009) Fluid evolution and metallogenic dynamics during

tectonic regime transition: an example from the Jiapigou gold belt in Northeast China. Res Geol 59(2):140–153
Deng JF, Mo XX, Zhao HL, Wu ZX, Luo ZH, Su SG (2004) A new model for the dynamic evolution of Chinese lithosphere: continental roots-plume tectonics. Earth-Sci Rev 65:223–275
Deng J, Yuan WM, Carranza EJM, Yang LQ, Wang CM, Yang LY, Hao NN (2014) Geochronology and thermochronometry of the Jiapigou gold belt, northeastern China: new evidence for multiple episodes of mineralization. J Asian Earth Sci 89:10–27
Fan GH, Li JW, Deng XD, Gao WS, Li SY (2021) Age and origin of the Dongping Au-Te deposit in the North China Craton revisited: evidence from paragenesis, geochemistry, and in situ U-Pb geochronology of garnet. Econ Geol 116(4):963–985
Fan HR, Xie YH, Zhai MG (2001) Hydrothermal fluids in the Dongping gold deposit, northwestern Hebei Province. Sci China Ser D 44:748–757
Fan JG, Ni P, Su WC, Qi L, Tian JH (2000) Characteristics and significance of rare earth elements in quartz of Sidaogou hydrothermal gold deposit. Liaoning Acta Petrologica Sinica 16(4):587–590 (in Chinese)
Fougerouse D, Micklethwaite S, Tomkins AG, Mei Y, Kilburn M, Guagliardo P, Fisher LA, Halfpenny A, Gee M, Paterson D, Howard DL (2016) Gold remobilisation and formation of high grade ore shoots driven by dissolution-reprecipitation replacement and Ni substitution into auriferous arsenopyrite. Geochim Cosmochim Acta 178:143–159
Fu JL, Hu ZC, Zhang W, Yang L, Liu YS, Li M, Zong KQ, Gao S, Hu SH (2016) In situ sulfur isotopes ($\delta^{34}S$ and $\delta^{33}S$) analyses in sulfides and elemental sulfur using high sensitivity cones combined with the addition of nitrogen by laser ablation MC-ICP-MS. Anal Chim Acta 911:14–26
Fu LB, Wei JH, Bagas L, Pirajno F, Zhao X, Chen JJ, Zhang DH, Chen Y, Chen Y (2020) Multistage exhumation of the Anjiayingzi gold deposit, northern North China Block: geodynamic settings and exploration implications. Ore Geol Rev. https://doi.org/10.1016/j.oregeorev.2019.103220
Gao Y, Nie FJ, Xiao W, Liu YF, Zhang WB, Wang FX (2014) Metallogenic age of the Changshanhao gold deposit in Inner Mongolia, China. Acta Petrologica Sinica 30(7):2092–2100
Gao S, Xu H, Zhang D, Shao H, Quan S (2015) Ore petrography and chemistry of the tellurides from the Dongping gold deposit, Hebei Province, China. Ore Geol Rev 64:23–34
Gao S, Xu H, Li SR, Santosh M, Zhang DS, Yang LJ, Quan SL (2017) Hydrothermal alteration and hydrothermal fluids associated with gold-tellurium mineralization in the Dongping gold deposit, China. Ore Geol Rev 80:166–184
Helt KM, Williams-Jones AE, Clark JR, Wing BA, Wares RP (2014) Constraints on the genesis of the Archean oxidized, intrusion-related Canadian Malartic gold deposit, Quebec, Canada-a reply. Econ Geol 109:2069–2071
Henderson P (1984) Rare earth element geochemistry. Elsevier Science Publishers, Amsterdam
Hodkiewicz PF, Groves DI, Davidson GJ et al (2009) Influence of structural setting on sulphur isotopes in Archean orogenic gold deposits, Eastern Goldfields Province, Yilgarn, Western Australia. Miner Depos 44:129–150
Hu ZC, Zhang W, Liu YS, Gao S, Li M, Zong KQ, Chen HH, Hu SH (2015) "Wave" signal-smoothing and mercury-removing device for laser ablation quadrupole and multiple collector ICPMS analysis: application to lead isotope analysis. Anal Chem 87:1152–1157
Huston DL, Sie SH, Suter GF, Cooke DR, Both RA (1995) Trace-elements in sulfide minerals from eastern Australian volcanic-hosted massive sulfide deposits: part 1. proton microprobe analyses of pyrite, chalcopyrite and sphalerite, *and* part 2. selenium levels in pyrite: comparison with $\delta^{34}S$ values and implications for the source of sulfur in volcanogenic hydrothermal systems. Econ Geol 90:1167–1196
Jia SS, Wang ED, Fu JF, Wu L, Zhao CF (2018) Indosinian gold mineralization and magmatic-hydrothermal evolution of the Hadamengou gold deposit at the northern margin of the North China Craton: constraints from K-feldspar laser Ar-40/Ar-39 dating. J Geochem Explor 190:314–324
Jiang N, Liu YS, Zhou WG, Yang JH, Zhang SQ (2007) Derivation of Mesozoic adakitic magmas from ancient lower crust in the North China craton. Geochim Cosmochim Acta 71:2591–2608
Jiang N, Zhang S, Zhou W, Li YS (2009) Origin of a Mesozoic granite with A-type characteristics from the North China craton: highly fractionated from I-type magmas? Contrib Mineral Petrol 158(1):113–130
Jiang SH, Nie FJ (2000) $^{40}Ar/^{39}Ar$ geochronology study on the alkaline intrusive complex and related gold deposits, northwestern Hebei, China. Geol Rev 46:621–627 (in Chinese with English abstract)
Jo J, Jeong Y, Shin D (2021) Regional variations of sulfur isotope compositions for metallic deposits in South Korea. Resour Geol 71(3):202–225
Keith M, Smith DJ, Jenkin GRT, Holwell DA, Dye MD (2018) A review of Te and Se systematics in hydrothermal pyrite from precious metal deposits: insights into ore-forming processes. Ore Geol Rev 96:269–282
Koglin N, Frimmel HE, Minter WEL, Bratz H (2010) Trace-element characteristics of different pyrite types in Mesoarchaean to Palaeoproterozoic placer deposits. Miner Deposita 45:259–280
Kong DX, Xu JF, Chen JL (2016) Oxygen isotope and trace element geochemistry of zircons from porphyry copper system: implications for Late Triassic metallogenesis within the Yidun Terrane, southeastern Tibetan Plateau. Chem Geol 441:148–161
LaFlamme C, Sugiono D, Thébaud N et al (2018) Multiple sulfur isotopes monitor fluid evolution of an Archean orogenic gold deposit. Geochim Cosmochim Acta 222:436–446
Large RR, Maslennikon VV, Robert F, Danyushevsky LV, Chang ZS (2007) Multistage sedimentary and metamorphic origin of pyrite and gold in the giant Sukhoi Log deposit, Lena gold province, Russia. Econ Geol 102:1233–1267
Large RR, Danyushevsky L, Hollit C, Maslennikov V, Meffre S, Gilbert S, Bull S, Scott R, Emsbo P, Thomas H, Singh B, Foster J (2009) Gold and trace element zonation in pyrite using a laser imaging technique: implications for the timing of gold in orogenic and Carlin-style sediment-hosted deposits. Econ Geol 104:635–668
Large RR, Meffre S, Burnett R, Guy B, Bull S, Gilbert S, Goemann K, Danyushevsky L (2013) Evidence for an intrabasinal source and multiple concentration processes in the formation of the Carbon Leader Reef, Witwatersrand Supergroup, South Africa. Econ Geol 108:1215–1241
Large RR, Halpin JA, Danyushevsky LV, Maslennikov VV, Bull SW, Long JA, Gregory DD, Lounejeva E, Lyons TW, Sack PJ, McGoldrick PJ, Calver CR (2014) Trace element content of sedimentary pyrite as a new proxy for deep-time ocean-atmosphere evolution. Earth Planet Sci Lett 389:209–220
Li CJ, Bao ZW, Zhao ZZ, Qiao YL (2012a) Zircon U-Pb age and Hf isotopic compositions of the granitic gneisses from the Sanggan complex in the Zhangjiakou area: constraints on the early evolution of North China Craton. Acta Petrol Sin 28:1057–1072 (in Chinese with English abstract)
Li CM, Deng JF, Su SG, Li HM, Liu XM (2010) Two stage zircon U-Pb ages of the potash altered rock in the Dongping gold

deposit, Hebei Province, and their geological implications. Acta Geoscientica Sinica 31:843–852

Li CM, Deng JF, Su SG, Liu XM (2012b) LA-ICP-MS zircon U-Pb age of the brittle-ductile shear zones in Hougou gold ore-field, Northwestern Hebei Province. Geotecton Metallog 36:157–167 (in Chinese with English abstract)

Li H, Watanabe K, Yonezu K (2014a) Zircon morphology, geochronology and trace element geochemistry of the granites from the Huangshaping polymetallic deposit, South China: implications for the magmatic evolution and mineralization processes. Ore Geol Rev 60:14–35

Li H, Li JW, Algeo TJ, Wu JH, Cisse M (2018a) Zircon indicators of fluid sources and ore genesis in a multi-stage hydrothermal system: the Dongping Au deposit in North China. Lithos 314:463–478

Li H, Wu JH, Evans NJ, Jiang WC, Zhou ZK (2018b) Zircon geochronology and geochemistry of the Xianghualing A-type granitic rocks: insights into multi-stage Sn polymetallic mineralization in South China. Lithos 312–313:1–20

Li HM, Shen YC, Mao JW, Liu TB, Zhu HP (2003) REE features of quartz and pyrite and their fluid inclusions: an example of Jiaojia-type gold deposits, northwestern Jiaodong peninsula. Acta Petrologica Sinica 19(2):267–274 (in Chinese)

Li HY, Zhang ZY, Li P, Xing GH (2000) Structural analysis and genesis of gold deposit in the Dongping. Geol Prospect 36(5):36–38 (in Chinese with English abstract)

Li JW, Bi SJ, Selby D, Chen L, Vasconcelos P, Thiede D, Zhou MF, Zhao XF, Li ZK, Qiu HN (2012c) Giant Mesozoic gold provinces related to the destruction of the North China Craton. Earth Planet Sci Lett 349:26–37

Li SR, Santosh M, Zhang HF, Shen JF, Dong GC, Wang JZ, Zhang JQ (2013) Inhomogeneous lithospheric thinning in the central North China Craton: zircon U-Pb and S-He-Ar isotopic record from magmatism and metallogeny in the Taihang Mountains. Gondwana Res 23:141–160

Li SR, Santosh M, Zhang HF, Luo JY, Zhang JQ, Li CL, Song JY, Zhang XB (2014b) Metallogeny in response to lithospheric thinning and craton destruction: geochemistry and U-Pb zircon chronology of the Yixingzhai gold deposit, central North China Craton. Ore Geol Rev 56:457–471

Li SZ (1999) Control of echelon vein on mineralization and its indication to prospecting. Geol Prospect (in Chinese with English abstract)35(6):15–18

Li W, Cook NJ, Xie GQ, Mao JW, Ciobanu CL, Li JW, Zhang ZY (2019) Textures and trace element signatures of pyrite and arsenopyrite from the Gutaishan Au-Sb deposit, South China. Miner Deposita 54:591–610

Liu ZF, Wang JM, Lv JB, Zheng GS (2006) Geological features and age of the Wenquan rapakivi granite, Chicheng County. Hebei Geol China 33:1052–1058 (in Chinese with English abstract)

Liu YS, Hu ZC, Gao S, Gunther D, Xu J, Gao CG, Chen HH (2008) In situ analysis of major and trace elements of anhydrous minerals by LA-ICP-MS without applying an internal standard. Chem Geol 257:34–43

Liu JP, Rong YN, Zhang SG, Liu ZF, Chen WK (2017) Indium mineralization in the Xianghualing Sn-polymetallic ore-field in southern Hunan, southern China. Minerals 7(9) art.173, 26 pp

Liu S, Chen B, Zheng J, Wu Y, Bao C, Zhao G (2022) A metamorphic devolatilization model for the genesis of the Baiyun gold deposit in the North China Craton: a novel Fe-S isotopes perspective. Gondwana Res 106:126–141

Loftus-Hills G, Solomon M (1967) Cobalt, nickel and selenium in sulphides as indicators of ore genesis. Miner Deposita 2:228–242

Luo Z, Miao L, Guan K, Giu Y, McNaughton NJ (2001) SHRIMP chronological study of Shuiquangou intrusive body in Zhangjiakou area, Hebei Province and its geochemical significance. Geochimica 30:116–122 (in Chinese)

Ma ZJ, Zhao JM (1999) Contrast research on Tianshan orogenic belt and Yinshan-Yanshan orogenic belt. Earth Sci Front 6:95–102 (in Chinese with English abstract)

Ma Q, Zheng JP, Griffin WL, Zhang M (2012) Triassic "adakitic" rocks in an extensional setting (North China): melts from the cratonic lower crust. Lithos 149:159–173

Ma Y, Jiang SY, Frimmel HE (2022) Deciphering multiple ore-forming processes of the Shuangqishan orogenic gold deposit, Southeast China by in situ analysis of pyrite. Ore Geol Rev 142. https://doi.org/10.1016/j.oregeorev.2022.104730

Mao JW, Li YQ, Goldfarb R, He Y, Zaw K (2003) Fluid inclusion and noble gas studies of the Dongping gold deposit, Hebei Province, China: a mantle connection for mineralization? Econ Geol Bull Soc 98:517–534

Mao JW, Wang YT, Li HM, Pirajno F, Zhang CQ, Wang RT (2008) The relationship of mantle-derived fluids to gold metallogenesis in the Jiaodong Peninsula: evidence from D-O-C-S isotope systematics. Ore Geol Rev 33:361–381

Mao GZ, Hua RM, Gao JF, Li WQ, Zhao KD, Long GM, Lu HJ (2009) Existing forms of REE in gold-bearing pyrite of the Jinshan gold deposit, Jiangxi Province, China. J Rare Earths 27:1079–1087

Miao LC, Qiu YM, McNaughton N, Luo ZK, Groves D, Zhai YS, Fan WM, Zhai MG, Guan K (2002) SHRIMP U-Pb zircon geochronology of granitoids from Dongping area, Hebei Province, China: constraints on tectonic evolution and geodynamic setting for gold metallogeny. Ore Geol Rev 19:187–204

Morey AA, Tomkins AG, Bierlein FP, Weinberg RF, Davidson GJ (2008) Bimodal distribution of gold in pyrite and arsenopyrite: examples from the Archean Boorara and Bardoc shear systems, Yilgarn craton, Western Australia. Econ Geol 103:599–614

Morishita Y, Shimada N, Shimada K (2018) Invisible gold in arsenian pyrite from the high-grade Hishikari gold deposit, Japan: significance of variation and distribution of Au/As ratios in pyrite. Ore Geol Rev 95:79–93

Mutschler FE, Griffin ME, Stevens DS, Shannon SS (1985) Precious metal deposits related to alkaline rocks in the North American Cordillera: an interpretive review. Geol Soc South Africa Trans 88:355–377

Nie FJ (1997) Type and distribution of gold deposits along the northern margin of the North China Craton, People's Republic of China. Int Geol Rev 39:151–180

Nie FJ (1998) Geology and origin of the Dongping alkalic-type gold deposit, Northern Hebei province, People's Republic of China. Resour Geol 48:139–158

Nie FJ, Jiang SH, Liu Y (2004) Intrusion-related gold deposits of North China craton, People's Republic of China. Resour Geol 54:299–324

Oberthuer T, Mumm AS, Vetter U et al (1996) Gold mineralization in the Ashanti Belt of Ghana; genetic constraints of the stable isotope geochemistry. Econ Geol 91:289–301

Ohmoto H, Rye RO (1979) Isotopes of sulfur and carbon. In: Barnes HL (ed.) Geochemistry of hydrothermal ore deposits. 2nd edn. New York, John Wiley & Sons Inc., pp 509–567

Phillips GN, Groves DI, Neall FB, Donnelly TH, Lambert IB (1986) Anomalous sulfur isotope compositions in the Golden Mile, Kalgoorlie. Econ Geol 81:2008–2015

Pokrovski GS, Tagirov BR, Schott J, Hazemann JL, Proux O (2009) A new view on gold speciation in sulfur-bearing hydrothermal fluids from in situ X-ray absorption spectroscopy and quantum-chemical modeling. Geochim Cosmochim Acta 73:5406–5427

Qiu YM, Gan SF, Hou G, Zhang ZS, Wang J (1993) On gold abundance of Archaean metamorphic rocks and genesis of gold deposits in North China Platform, P.R China. Res Geol 16:351–357

Reich M, Kesler SE, Utsunomiya S, Palenik CS, Chryssoulis SL, Ewing RC (2005) Solubility of gold in arsenian pyrite. Geochim Cosmochim Acta 69:2781–2796

Reich M, Deditius A, Chryssoulis S, Li JW, Ma CQ, Parada MA, Barra F, Mittermayr F (2013) Pyrite as a record of hydrothermal fluid evolution in a porphyry copper system: a SIMS/EMPA trace element study. Geochim Cosmochim Acta 104:42–62

Richards JP, Kerrich R (1993) The Porgera gold mine, Papua New Guinea: magmatic-hydrothermal to epithermal evolution of an alkalic-type precious metal deposit. Econ Geol 88:1017–1052

Shannon RD (1976) Revised effective ionic radii and systematics studies of interatomic distances in halides and chalcogenides. Acta Crystallogr A 32(5):751–767

Shao JA, Han QJ, Zhang LQ, Mu BL (1999) Cumulate complex xenoliths in the early Mesozoic in eastern Inner Mongolia. Chin Sci Bull 44(14):1272–1279

She HQ, Wang YW, Li QH, Zhang DQ, Feng CY, Li DX (2006) The mafic granulite xenoliths and its implications to mineralization in Chaihulanzi gold deposit, Inner Mongolian, China. Acta Geological Sinica 80(6):863–874 (In Chinese with English abstract)

Simon G, Huang H, Penner-Hahn JE, Kesler SE, Kao LS (1999) Oxidation state of gold and arsenic in gold-bearing arsenian pyrite. Am Miner 84:1071–1079

Song GX (1991) A gold deposit associated with alkali-complex rocks. Geol Prospect 27(8):1–8 (in Chinese with English abstract)

Song GR, Zhao ZH (1996) Geology of Dongping alkaline complex-hosted gold deposit in Hebei Province. Seismological Press, Beijing, pp 1–170 (in Chinese with English abstract)

Sun SS, McDonough WF (1989) Chemical and isotopic systematics of oceanic basalts: implications for mantle composition and processes. In: Saunders, A.D., Norry, M.J. (Eds.), Magmatism in the ocean basins. Geol. Soc. London, London, pp. 313–345

Sung YH, Brugger J, Ciobanu CL, Pring A, Skinner W, Nugus M (2009) Invisible gold in arsenian pyrite and arsenopyrite from a multistage Archaean gold deposit: Sunrise Dam, Eastern Goldfields Province, Western Australia. Miner Deposita 44:765–791

Tanner D, Henley RW, Mavrogenes JA, Holden P (2016) Sulfur isotope and trace element systematics of zoned pyrite crystals from the El Indio Au-Cu-Ag deposit, Chile. Contrib Mineral Petrol 171(33):17

Thomas HV, Large RE, Bull SW, Maslennikov V, Berry RF, Fraser R, Froud S, Moye R (2011) Pyrite and pyrrhotite textures and composition in sediments, laminated quartz veins, and reefs at Bendigo Gold Mine, Australia: insights for ore genesis. Econ Geol 106:1–31

Thompson TB, Trippel AD, Dwelley PC (1985) Mineralized veins and breccias of the Cripple Creek district, Colorado. Econ Geol 80:1669–1688

Ulrich T, Long DGF, Kamber BS, Whitehouse MJ (2011) In situ trace element and sulfur isotope analysis of pyrite in a Paleoproterozoic gold placer deposit, Pardo and Clement Townships, Ontario, Canada. Econ Geol 106:667–686

Velasquez G, Beziat D, Salvi S, Siebenaller L, Borisova AY, Pokrovski GS, de Parseval P (2014) Formation and deformation of pyrite and implications for gold mineralization in the El Callao District, Venezuela. Econ Geol 109:457–486

Wang Y, Jiang XM, Wang ZK (1990) Characteristics of lead and sulfur isotope of the gold deposits in Zhangjiakou Xuanhua area, Hebei Province. Contrib Geol Miner Resour Res 5(2):66–75 (in Chinese with English abstract)

Wang SL, Wang JB, Peng SL, Guo ZL, Qiu YJ (2004) REE geochemistry of ore fluids in the Koktag lead-zinc deposit, Xinjiang. Geol China 31(3):308–314 (in Chinese)

Wang QF, Deng J, Zhao JC, Li N, Wan L (2012) The fractal relationship between orebody tonnage and thickness. J Geochem Explor 122:4–8

Wang DZ, Liu J, Carranza EJM, Zhai D, Wang Y, Zhen S, Wang J, Wang J, Liu Z, Zhang F (2019a) Formation and evolution of snowball quartz phenocrysts in the Dongping porphyritic granite, Hebei Province, China: insights from fluid inclusions, cathodoluminescence, trace elements, and crystal size distribution study. Lithos 340–341:239–254

Wang DZ, Liu JJ, Zhai DG, Zhen SM, Wang J, Yang X (2019b) New discovery of molybdenite in the Dongping Gold Deposit, Hebei Province, China and its Re-Os geochronological implications. Acta Geol Sin (engl Ed) 93:769–770

Werle JL, Ikramuddin M, Mutschler FE (1984) Allard Stock, La Plata Mountains, Colorado – an alkaline rock-hosted porphyry copper-precious metal deposit. Canad Jour Earth Sci 21:630–641

Wu YF, Evans K, Li JW, Fougerouse D, Large RR, Guagliardo P (2019) Metal remobilization and ore-fluid perturbation during episodic replacement of auriferous pyrite from an epizonal orogenic gold deposit. Geochim Cosmochim Acta 245:98–117

Xing WW, Li F, Liu XH, Yang YS, Cheng Y (2011) Characteristics and mineralization of Shuijingtun gold deposit in Chongli county, Hebei Province. Gansu Geology 20(2):51–59 (in Chinese with English abstract)

Yang LQ, Deng J, Wang ZL, Guo LN, Li RH, Groves DI, Danyushevsky LV, Zhang C, Zheng XL, Zhao H (2016) Relationships between gold and pyrite at the Xincheng Gold Deposit, Jiaodong Peninsula, China: implications for gold source and deposition in a brittle epizonal environment. Econ Geol 111:105–126

Yin JZ (1994) S isotopic features of the major gold deposits in the Northwestern Hebei Province. Gold Sci Technol 2(3):33–39 (in Chinese)

Yuan Q, Ge WS, Ding H, Chen J, Jia HX, Huang G, Zhang JR (2017) Geochemical characteristics of REE and trace elements of pyrite: constraint on the ore-forming fluid of the Lvyuan gold deposit, Eastern Junggar. Bull Mineral Petrol Geochem 36(4):628–636 (in Chinese with English abstract)

Zartman RE, Haines SM (1988) The plumbotectonic model for Pb isotopic systematics among major terrestrial reservoirs—a case for bi-directional transport. Geochim Cosmochim Acta 52:1327–1339

Zhai D, Williams-Jones AE, Liu J et al (2018) Mineralogical, fluid inclusion, and multiple isotope (HOS-Pb) constraints on the genesis of the Sandaowanzi epithermal Au-Ag-Te deposit, NE China. Econ Geol 113:1359–1382

Zhang SH, Yue Z, Liu J, Hu JM, Chen ZL, Li M, Pei JL, Chen ZY, Zhou JX (2007) Emplacement depths of the Late Paleozoic Mesozoic granitoid intrusions from the northern North China block and their tectonic implications. Acta Petrol Sin 23:625–638

Zhang SH, Zhao Y, Liu XC, Liu DY, Chen FK, Xie LW, Chen HH (2009) Late Paleozoic to Early Mesozoic mafic–ultramafic complexes from the northern North China Block: constraints on the composition and evolution of the lithospheric mantle. Lithos 110(1–4):229–246

Zhang XH, Zhang HF, Jiang N, Zhai MG, Zhang YB (2010) Early Devonian alkaline intrusive complex from the northern North China craton: a petrological monitor of post-collisional tectonics. J Geol Soc London 167:717–730

Zhang XH, Mao Q, Zhang HF, Zhai MG, Yang YH, Hu ZC (2011) Mafic and felsic magma interaction during the construction of high-K calc-alkaline plutons within a metacratonic passive margin: the Early Permian Guyang batholith from the northern North China Craton. Lithos 125:569–591

Zhang WB, Hou WR, Nie FJ (2013) Re-Os age dating of the Hadamengou Au deposit, Inner Mongolia, China and its geological significance. Mineral Deposit Res High-Tech World 1–4:1219–1222

Zhang J, Deng J, Chen H-Y et al (2014) LA-ICP-MS trace element analysis of pyrite from the Chang'an gold deposit, Sanjiang region, China: implication for ore-forming process. Gondwana Research 26(2):557–575

Zhang W, Hu ZC, Gunther D, Liu YS, Ling WL, Zong KQ, Chen HH, Gao S (2016) Direct lead isotope analysis in Hg-rich sulfides by LA-MC-ICP-MS with a gas exchange device and matrix-matched calibration. Anal Chim Acta 948:9–18

Zhang YY, Zhen SM, Wang DZ, Liu JJ, Wang J, Zha ZJ, Bai HJ (2022) In situ trace elements and sulfur isotopes of sulfides in the Dabaiyang Te-Au deposit, Hebei Province, China: implications for Au remobilization from pyrite. Ore Geol Rev 140. https://doi.org/10.1016/j.oregeorev.2021.104626

Zhao ZH, Bao ZW, Qiao YL (2010) A peculiar composite M- and W-type REE tetrad effect: evidence from the Shuiquangou alkaline syenite complex, Hebei Province, China. Chin Sci Bull 55:2684–2696

Zhou LY, Wang Y (2012) Late carboniferous syn-tectonic magmatic flow at the northern margin of the North China craton—evidence for the reactivation of cratonic basement. J Asian Earth Sci 54–55:131–142

Zong KQ, Klemd R, Yuan Y, He ZY, Guo JL, Shi XL, Liu YS, Hu ZC, Zhang ZM (2017) The assembly of Rodinia: the correlation of early Neoproterozoic (ca. 900 Ma) high-grade metamorphism and continental arc formation in the southern Beishan Orogen, southern Central Asian Orogenic Belt (CAOB). Precambrian Res 290:32–48